



# On the advantages of mixed formulation and higher-order elements for computational morphoelasticity

Chennakesava Kadapa<sup>a</sup>, Zhanfeng Li<sup>b</sup>, Mokarram Hossain<sup>c,\*</sup>, Jiong Wang<sup>b</sup>

<sup>a</sup> School of Engineering, University of Bolton, Bolton, United Kingdom

<sup>b</sup> School of Civil Engineering and Transportation, South China University of Technology, Guangdong, China

<sup>c</sup> Zienkiewicz Centre for Computational Engineering (ZCCE), Swansea University, Swansea, United Kingdom

## ARTICLE INFO

### Keywords:

Growth-induced deformations  
Finite element analysis  
Mixed formulation  
Hyperelasticity  
Morphoelasticity

## ABSTRACT

In this paper, we present a mixed displacement–pressure finite element formulation that can successively model compressible as well as truly incompressible behaviour in growth-induced deformations significantly observed in soft materials. Inf-sup stable elements of various shapes based on quadratic Bézier elements are employed for spatial discretisation. At first, the capability of the proposed framework to accurately model finite-strain growth-induced deformations is illustrated using several examples of plate models in which numerical results are directly compared with analytical solutions. The framework is also compared with the classical Q1/P0 finite element that has been used extensively for simulating the deformation behaviour of soft materials using the quasi-incompressibility assumption. The comparisons clearly demonstrate the superior capabilities of the proposed framework. Later, the effect of hyperelastic constitutive models and compressibility on the growth-induced deformation is also studied using the example of a bilayered strip in three dimensions. Finally, the potential of the proposed finite element framework to simulate growth-induced deformations in complex three-dimensional problems is illustrated using the models of flower petals, morphoelastic rods, and thin cylindrical tubes.

## 1. Introduction

The growth (or atrophy) of soft biological tissues such as leaves, petals and skin are commonly observed in nature. Due to the inhomogeneous and incompatible growth fields, which is referred to as the differential growth, soft tissues usually exhibit various geometrical shape changes and different kinds of morphological patterns. Such morphogenesis of soft living tissues could render various instabilities that have either a positive outcome such as the cortical folding in the brain and wrinkling of skin or affect adversely such as folding of asthmatic airways (Armstrong et al., 2016; Kuhl, 2014; Budday et al., 2014). Moreover, any anomalies in growing tissues may create instabilities which could result in fatal health conditions (Raybaud and Widjaja, 2011). Therefore, experimental study and numerical simulations of such phenomena have attracted extensive research interests during the past years (Ambrosi et al., 2011; Li et al., 2012; Xu et al., 2020). Besides the factors of genetic (Nath et al., 2003; Coen et al., 2004) and biochemistry (Green, 1996), it is now understood that the mechanical effects play an important role in the growth-induced deformations of soft biological tissues (Budday et al., 2014; Skalak et al., 1996; Lubarda and Hoger, 2002; Ben Amar and Goriely, 2005; Dervaux et al., 2009; Rausch and Kuhl, 2013). In the engineering fields, the growth (e.g., swelling) effects of

\* Corresponding author.

E-mail addresses: [c.kadapa@bolton.ac.uk](mailto:c.kadapa@bolton.ac.uk) (C. Kadapa), [ctzf.li@mail.scut.edu.cn](mailto:ctzf.li@mail.scut.edu.cn) (Z. Li), [mokarram.hossain@swansea.ac.uk](mailto:mokarram.hossain@swansea.ac.uk) (M. Hossain), [ctjwang@scut.edu.cn](mailto:ctjwang@scut.edu.cn) (J. Wang).

<https://doi.org/10.1016/j.jmps.2020.104289>

Received 14 October 2020; Received in revised form 7 December 2020; Accepted 24 December 2020

Available online 29 December 2020

0022-5096/© 2020 Elsevier Ltd. All rights reserved.

soft material (e.g., polymers, hydrogels) samples have also been potentially utilised for the manufacture of soft intelligent devices, e.g., actuators, soft robotics, microfluidic devices, flexible electronics, artificial muscles, smart morphable surfaces in aerodynamics, drug delivery (Ionov, 2013; Yuk et al., 2017; Khang et al., 2009; Stafford et al., 2004; Terwagne et al., 2014), to mention a few. With the help of elaborated design of the compositions or architectures in soft material samples, various structures can be fabricated using differential growth, which is widely known as ‘shape-programming’ of soft material samples (Kempaiah and Nie, 2014; Liu et al., 2016).

At the continuum level, the nonlinear elasticity theory (Ogden, 1997) provides a solid framework for modelling the growth-induced deformations of soft materials, see Kuhl (2014), Kuhl et al. (2003), Jones and Chapman (2012) for exhaustive reviews. Usually, the approach proposed by Rodriguez et al. (1994) is followed, in which the total deformation gradient tensor is decomposed multiplicatively into an elastic deformation gradient tensor (representing the elastic response of the material) and a growth tensor (representing the changes of body volume/mass). To describe the elastic behaviour of soft materials, some suitable hyperelastic model must be adopted (e.g., Neo-Hookean, Mooney–Rivlin, Ogden), see Hossain and Steinmann (2013), Hossain et al. (2015) and Steinmann et al. (2012). Furthermore, as the elastic response of soft materials is generally volumetric incompressible, an additional constraint equation of incompressibility also needs to be incorporated. The evolution laws of the growth tensor can be proposed based on some phenomenological or micromechanical models (Kuhl, 2014; Lanir, 2015). While, by considering the fact that the time-scale of growth is much greater than that of the elastic wave propagation, the growth tensor can also be treated as a known function of given input parameters (Kuhl, 2014).

Along with the large deformation behaviour, mechanical instabilities such as buckling, wrinkling, folding and creasing are commonly observed in growth-induced deformation of soft materials (Zhao et al., 2015; Budday et al., 2017; Zhou et al., 2018). In the existing theoretical works, at first, the instability phenomena in soft material samples have been studied systematically through the linear or post-buckling bifurcation analyses (Ben Amar and Goriely, 2005; Audoly and Boudaoud, 2008; Cai et al., 2011; Cao and Hutchinson, 2012; Li et al., 2013; Xu et al., 2014, 2015; Holmes, 2019). For instance, Sultan and Boudaoud (2008) experimentally investigated the post-buckling behaviour of a swollen thin gel layer bound to a compliant substrate. They further measured the wavelengths and amplitudes of the resulting modes that were compared with a simplified model of a self-avoiding rod that resulted in good agreements. In order to mimic some common phenomena in biological tissues such as mucosal folding, Moulton and Goriely (2011) investigated the circumferential buckling instability of a growing cylindrical tube under a uniform radial external pressure. They found that a change in thickness due to the growth can have a dramatic impact on the circumferential buckling, both in the critical pressure and the buckling pattern. Holmes et al. (2011) studied swelling-induced bending and twisting of soft thin elastic plates. Pezulla et al. (2016) studied the mechanics of thin growing bilayers. In addition to analyses of growth-induced deformations in biological tissues and plants, efforts have also been made to find similar phenomena in soft polymeric materials such in gels (e.g., hydrogels and smart responsive gels). For instance, Mora and Boudaoud (2006) experimentally and theoretically investigated the pattern formations arising from the differential swelling of gels. However, formulations of their models are based on small strain theory using the equations of thin plates.

Soft material samples in nature or in engineering applications usually have thin plate forms. To study the mechanical behaviours of these plate samples, one needs to adopt a suitable plate model. Many of the previous works were conducted based on the well-known Föppl von Kármán (FvK) plate theory (Dervaux et al., 2009; Cai et al., 2011; Budday et al., 2014). However, developed under the assumption of linear constitutive law, the FvK plate theory has limited applicability to modelling large deformation behaviour in soft materials. In our previous works such as in Dai and Song (2014) and Wang et al. (2016), a finite-strain plate theory was proposed for both compressible and fully incompressible hyperelastic materials, which can achieve the term-wise consistency with the three-dimensional (3D) stationary potential energy and there is no need to propose any ad-hoc assumptions on the deformation of the plate. Recently, in Wang et al. (2019) and Du et al. (2020), the material’s growth effects are further incorporated in the finite-strain plate theory, such that the theory can be applicable for studying the growth-induced deformations of thin hyperelastic plates. Based on this finite-strain plate theory, the growth-induced deformations of single- or multiple-layered hyperelastic plate have been studied (Wang et al., 2019; Du et al., 2020).

The numerical treatments for simulating growth-phenomena have been actively investigated over the years. Ilseng et al. (2019) numerically investigated the buckling initiation on layered hydrogels during transient diffusion. For this, they used the displacement-based finite element method (FEM) within the commercial software package Abaqus. Based on the finite element analysis results, they concluded that the initiation of buckling in a layered hydrogel structure is highly affected by transient swelling effects. Similarly, Xu et al. (2014, 2015), in a series of papers, investigated the growth-induced instabilities in thin films compliant to hyperelastic substrates using finite element method. For that, they used nonlinear shell formulation for the film and a displacement-based FEM for the substrate. Moreover, in order to predict a sequence of secondary bifurcations on the post-buckling evolution paths, they used the so-called Asymptotic Numerical Method. In contrast to finite element-based approaches, Dortdivanlioglu and Linder (2019) and Dortdivanlioglu et al. (2017) developed an isogeometric analysis (IGA)-based computational framework suitable to study morphological instabilities produced by growth-induced deformations. Recently, Wang et al. (2020) proposed NURBS-based isogeometric formulation to predict the mechanical behaviour of swellable soft materials. They addressed the well-known issue of volumetric locking as a result of the incompressibility of soft materials by adapting the  $F$ -bar projection method.

In the theoretical developments as well as in exploring the analytical solutions of growth-induced deformation problems, the elastic part of the deformation is assumed to be incompressible, see Wang et al. (2016, 2018a,b), Du et al. (2020), Moulton et al. (2020), Garcia-Gonzalez et al. (2018) and Garcia-Gonzalez and Jerusalem (2019). Yet, despite significant advances in the area of numerical computations of the growth-induced phenomena, incompressibility is one of the aspects that has not been given due consideration in the literature on computational modelling of the problem. To the best of the authors’ knowledge, only such finite

element formulations based on the quasi-incompressible approach in which incompressibility is enforced weakly are considered in the literature. Among such methods, the reduced-integration element in Abaqus or the Q1/P0 element are widely used in the literature. The difficulties associated with computational modelling of true incompressibility in growth problems are alluded briefly in a remark in [Menzel and Kuhl \(2012\)](#). Numerical treatment of the incompressibility constraint using a Lagrange multiplier is briefly discussed in [Nash and Hunter \(2000\)](#) without all the essential details related to the formulation such as basis functions for the pressure field, inf-sup stability condition for the displacement–pressure combination, accuracy and computational efficiency. Our present contribution aims to address the gap in computer modelling of incompressible deformations in growth problems by adapting a mixed displacement–pressure finite element formulation ([Kadapa, 2014](#); [Kadapa et al., 2016](#); [Kadapa, 2019b](#); [Kadapa and Hossain, 2020a,b](#)). The proposed formulation is applicable to compressible, nearly incompressible as well as to fully incompressible materials in growth-induced deformation problems.

The paper is organised as follows. After introducing the governing equations in Section 2 and presenting the formulation in Section 3, the accuracy of the proposed elements is compared against analytical results in Section 4. At the same time, the superior performance of the proposed framework is demonstrated by comparing it with some other classical FE formulations (e.g., Q1P0) used in simulating nearly incompressible materials. Later, the effect of different constitutive models and compressibility on the extent of deformation is studied in Section 5. Finally, the framework is used to simulate some complex three-dimensional soft structures triggered by growth-induced phenomena in Section 6.

## 2. Governing equations

### 2.1. Kinematics

Consider an arbitrary solid body with  $B_0$  as its reference configuration. Under the influence of external and/or internal forces, the body assumes a new configuration, say  $B_t$ . The new configuration can be represented with a mapping  $\mathcal{X} : B_0 \rightarrow B_t$ , that takes a point  $X \in B_0$  to a point  $x \in B_t$ . Following this, the new configuration,  $B_t$ , can be identified by a displacement field from the initial configuration,  $B_0$ . The displacement field in material coordinates is defined as

$$u(X) := \mathcal{X}(X) - X = x(X) - X. \quad (1)$$

Now, using the definition of the displacement field in (1), the total deformation gradient tensor,  $F$ , and its determinant,  $J$ , are given as

$$F := \frac{\partial x}{\partial X} = I + \frac{\partial u}{\partial X}, \quad \text{and} \quad J := \det(F), \quad (2)$$

where,  $I$  is the second-order identity tensor.

Following [Rodriguez et al. \(1994\)](#), the total deformation gradient tensor for the growth-induced deformation problem is multiplicatively decomposed into elastic part,  $F^e$ , and growth part,  $F^g$ , as

$$F = F^e F^g; \quad \text{or} \quad F_{iL} = F_{iS}^e F_{SL}^g \quad \text{for} \quad i, L, S = 1, 2, 3. \quad (3)$$

This decomposition assumes a stress-free intermediate configuration, say  $B_g$ , that consists of deformation due to pure material growth from the original pre-grown configuration  $B_0$ . The elastic part of the deformation gradient,  $F^e$ , accounts for the pure elastic deformations in the material and the growth tensor,  $F^g$ , accounts for the effects of pure volumetric deformations. The growth tensor,  $F^g$ , can be either isotropic or transversely isotropic or orthotropic or completely anisotropic, see [Menzel and Kuhl \(2012\)](#) for more details. For the isotropic case,  $F^g$  is given as

$$F^g = [1 + g] I, \quad (4)$$

where,  $g$  is a scalar quantity. A positive value of  $g$  results in material growth and a negative value results in atrophy aka shrinkage, see [Hossain et al. \(2010\)](#).

From Eq. (3), it follows that

$$J = J^e J^g, \quad (5)$$

where,

$$J = \det(F) > 0; \quad J^e = \det(F^e) > 0; \quad \text{and} \quad J^g = \det(F^g) > 0. \quad (6)$$

In the theoretical developments of growth-induced deformation problems, the elastic deformations are assumed to be incompressible; that is, the material does not undergo any change in the volume under pure elastic deformation. This incompressibility constraint can be expressed mathematically as,

$$J^e = 1. \quad (7)$$

2.1.1. Modifications for the incompressible cases

For computational modelling of incompressible deformations in finite strains, the strain and stress measures, and the energy density function ( $\Psi$ ) need to undergo appropriate modifications, see Zienkiewicz et al. (2014), Bonet and Wood (1997) and Ogden (1997) for the details. Accordingly, the elastic part of the deformation gradient,  $F^e$ , is decomposed multiplicatively into deviatoric and volumetric parts,  $F_{dev}^e$  and  $F_{vol}^e$ , respectively, as,

$$F^e = F_{vol}^e F_{dev}^e, \tag{8}$$

with

$$F_{vol}^e := J^{e1/3} I, \quad \text{and} \quad F_{dev}^e := J^{e-1/3} F^e. \tag{9}$$

We can now define the modified versions of the elastic deformation gradient tensor and the right Cauchy–Green tensor as

$$\bar{F}^e := J^{e-1/3} F^e; \quad \text{and} \quad \bar{C}^e := \bar{F}^{eT} \bar{F}^e. \tag{10}$$

Using Eq. (10)<sub>1</sub>, the total deformation gradient becomes

$$F = F^e F^g = J^{e1/3} \bar{F}^e F^g. \tag{11}$$

2.2. Constitutive models and stress–strain relations

Since the intermediate configuration consists of material growth or shrinkage only, it is stress-free. Therefore, the strain–energy density function,  $\Psi$ , is a function of the elastic part of the deformation gradient tensor,  $F^e$ , only, i.e.,

$$\Psi = \Psi(F, F^g) = \Psi(F^e). \tag{12}$$

For modelling the nearly or truly incompressible behaviour, it has been customary to additively decompose the strain–energy density function for hyperelastic materials into a deviatoric part,  $\Psi^{dev}$ , and a volumetric part,  $\Psi^{vol}$ , as

$$\Psi(\bar{C}^e, J^e) = \Psi^{dev}(\bar{C}^e) + \Psi^{vol}(J^e), \tag{13}$$

in which the volumetric energy function,  $\Psi^{vol}$ , vanishes for the truly incompressible case. To model the nearly incompressible and compressible deformation behaviour, several functions have been explored for  $\Psi^{vol}$ , see Kadapa and Hossain (2020a) and references therein. The deviatoric part can be any of the hyperelastic constitutive models, for example, Neo-Hookean, Ogden, Gent, Mooney–Rivlin, etc., see Hossain and Steinmann (2013), Hossain et al. (2015) and Steinmann et al. (2012) for the details. In the literature on analytical solutions for growth problems (Wang et al., 2016, 2018a,b; Du et al., 2020; Moulton et al., 2020),  $\Psi^{dev}$  is limited to the Neo-Hookean and Mooney–Rivlin models because of their simplicity and the ease of finding analytical solutions. However, the flexibility of the proposed finite element framework does not pose any restrictions on the type of strain–energy density function.

Now, the first Piola–Kirchhoff stress ( $\bar{P}^e$ ), Cauchy stress ( $\bar{\sigma}^e$ ) and the spatial tangent tensor ( $\bar{d}$ ) corresponding to the deviatoric part of the elastic energy function  $\Psi^{dev}$  can be computed as,

$$\bar{P}_{iJ}^e = \frac{\partial \Psi^{dev}(\bar{C}^e)}{\partial F_{iJ}^e}, \tag{14}$$

$$\bar{\sigma}_{ij}^e = \frac{1}{J^e} \bar{P}_{iJ}^e F_{jJ}^e, \tag{15}$$

$$\bar{d}_{ijkl}^e = \frac{1}{J^e} \bar{D}_{iJkL}^e F_{jJ}^e F_{lL}^e, \tag{16}$$

where,

$$\bar{D}_{iJkL}^e = \frac{\partial \bar{P}_{iJ}^e}{\partial F_{kL}^e}. \tag{17}$$

Using the above definitions, the effective first Piola–Kirchhoff stress ( $\hat{P}^e$ ) and the effective Cauchy stress ( $\hat{\sigma}^e$ ) for the mixed displacement–pressure formulation for the case of pure elastic deformation become

$$\hat{P}_{iJ}^e = \bar{P}_{iJ}^e + p J^e F_{iJ}^{e-1}, \tag{18}$$

$$\hat{\sigma}_{ij}^e = \frac{1}{J^e} \hat{P}_{iJ}^e F_{jJ}^e = \bar{\sigma}_{ij}^e + p \delta_{ij}, \tag{19}$$

where, the scalar  $p$  is the hydrostatic pressure, which is computed as an independent approximation. In the context of the mixed formulation,  $p$  is a Lagrange multiplier enforcing the incompressibility constraint (7) for the truly incompressible case. For the other cases, the constraint is modified accordingly, see Kadapa and Hossain (2020a).

If the material undergoes pure elastic deformation only, then the above expressions are sufficient. However, for modelling the combined elastic and growth-induced deformations, we need the derivatives of  $\Psi^{dev}$  with respect to total deformation gradient  $F$ . The first and second derivatives of  $\Psi^{dev}$  with respect to  $F$  are given by

$$\bar{P}_{iJ}^e = \frac{\partial \Psi^{dev}}{\partial F_{iJ}^e} = \frac{\partial \Psi^{dev}}{\partial F_{pQ}^e} \frac{\partial F_{pQ}^e}{\partial F_{iJ}^e} = \bar{P}_{pQ}^e \frac{\partial (F_{pR} F_{RQ}^{g-1})}{\partial F_{iJ}^e} = \bar{P}_{iQ}^e F_{JQ}^{g-1}, \tag{20}$$

$$\overline{\mathbb{D}}_{ijkl} = \frac{\partial^2 \Psi^{\text{dev}}}{\partial F_{kl} \partial F_{ij}} = \frac{\partial(\overline{P}_{iQ} F_{jQ}^{g^{-1}})}{\partial F_{kl}} = \frac{\partial \overline{P}_{iQ}}{\partial F_{mN}} \frac{\partial F_{mN}^e}{\partial F_{kl}} F_{jQ}^{g^{-1}} = \overline{\mathbb{D}}_{iQkN}^e F_{LN}^{g^{-1}} F_{jQ}^{g^{-1}}, \tag{21}$$

Finally, the total effective first Piola–Kirchhoff stress ( $\hat{P}$ ) and the effective Cauchy stress ( $\hat{\sigma}$ ) for the mixed displacement–pressure formulation for the combined elastic and growth-induced deformations are given as

$$\hat{P}_{iJ} = J^g \hat{P}_{iQ}^e F_{jQ}^{g^{-1}}; \quad \text{or} \quad \hat{P} = J^g \hat{P}^e F^{g^{-T}}, \tag{22}$$

$$\hat{\sigma}_{ij} = \frac{1}{J} \hat{P}_{iJ} F_{jJ} = \hat{\sigma}_{ij}^e; \quad \text{or} \quad \hat{\sigma} = \frac{1}{J} \hat{P} F^T = \hat{\sigma}^e. \tag{23}$$

### 2.3. Governing equations for growth problems

The equilibrium equations for nonlinear elastostatics of growth-induced deformation problem in the original pre-grown configuration ( $B_0$ ) can be written as,

$$-\nabla_X \cdot \hat{P} = f_0 \quad \text{in} \quad B_0 \tag{24}$$

$$u = \bar{u} \quad \text{on} \quad \partial B_0^D \tag{25}$$

$$\hat{P} \cdot n_0 = \bar{t} \quad \text{on} \quad \partial B_0^N \tag{26}$$

where,  $\nabla_X$  is the gradient operator with respect to the original configuration,  $f_0$  is the body force per unit undeformed volume,  $\bar{u}$  is the prescribed displacement on the Dirichlet boundary  $\partial B_0^D$ ,  $\bar{t}$  is the prescribed traction on the Neumann boundary  $\partial B_0^N$ , and  $n_0$  is the unit outward normal on the boundary  $\partial B_0$ .

### 3. Mixed displacement–pressure formulation for growth

The mixed displacement–pressure formulation recently proposed by the authors in Kadapa and Hossain (2020a) for the hyperelastic case is extended to growth-induced deformation problems in this work. The advantage of the adapted formulation is that (i) it is applicable for compressible as well as nearly and truly incompressible cases and (ii) results in symmetric global stiffness matrix irrespective of the volumetric energy function.

Following Kadapa and Hossain (2020a), the total energy functional for the equilibrium problem of the growth-induced deformation is given by,

$$\Pi(u, p) = \int_{B_0} \left[ \Psi^{\text{dev}}(\overline{C}^e) + \Psi_p(J^e, p) \right] J^g dV - \Pi_{\text{ext}}, \tag{27}$$

where,

$$\Pi_{\text{ext}} = \int_{B_0} u^T f_0 J^g dV + \int_{\partial B_0^N} u^T \bar{t} A^g dA \tag{28}$$

with  $A^g$  is the surface Jacobian due to growth. The factor  $J^g$  in Eq. (27) is due to the fact the integral is with respect to the original pre-grown configuration  $B_0$  (Moulton et al., 2020).

Note that  $\Psi_p(J^e, p)$  in Eq. (27) is different from the volumetric energy function,  $\Psi^{\text{vol}}$ ; this is primarily due to the fact that the  $\Psi^{\text{vol}}$  vanishes for the truly incompressible case. Here,  $\Psi_p$  is the generic energy functional that accounts for the effect of volumetric deformation in the compressible as well as incompressible regime. For the truly incompressible case,  $\Psi_p$  enforces the incompressibility constraint  $J^e=1$  using the Lagrange multiplier approach. With  $p$  as the Lagrange multiplier, we get

$$\Psi_p(J^e, p) = p [J^e - 1]. \tag{29}$$

For the compressible case,  $\Psi_p$  incorporates the volumetric energy function  $\Psi^{\text{vol}}$  using a more generic constraint. Following Kadapa and Hossain (2020a),  $\Psi_p$  for the generic case is given as,

$$\Psi_p(J^e, p) = p \left[ J^e - \hat{J} - \frac{\hat{\theta} p}{2} \right] \tag{30}$$

where,

$$\hat{J} = J_n^e - \frac{\partial \Psi^{\text{vol}}(J^e)}{\partial J^e} \Big|_{J_n^e}; \quad \hat{\theta} = \frac{1}{\frac{\partial^2 \Psi^{\text{vol}}(J^e)}{\partial J^{e2}} \Big|_{J_n^e}}, \tag{31}$$

with  $J_n^e = \det(F^e(u_n))$ . Here,  $n$  is the previously converged load step. The expression (30) is so generic that it simplifies to the one in (29) for the truly incompressible case for  $\hat{J} = 1$  and  $\hat{\theta} = 0$ . Thus the mixed formulation adapted in the present work is generic for both the compressible and incompressible cases. For the comprehensive details on the mixed formulation adapted in this work, we refer the reader to Kadapa and Hossain (2020a).

Taking the first variation ( $\delta$ ) of the total energy functional given in Eq. (27), we get,

$$\delta \Pi = \int_{B_0} \left[ \delta F_{iJ} \bar{P}_{iJ} J^g + \delta J p + \delta p \left[ J - J^g \hat{J} - J^g \hat{p} \right] \right] dV - \delta \Pi_{\text{ext}}, \tag{32}$$

which, after using the relations,

$$\delta F_{iJ} = \delta u_{i,j} F_{jJ}, \tag{33}$$

$$\delta J = J F_{ji}^{-1} \delta F_{iJ} = J \delta u_{i,j} \delta_{ij}, \tag{34}$$

can be written as,

$$\delta \Pi = \int_{B_0} \left[ \delta u_{i,j} \left[ \bar{\sigma}_{ij}^e + p \delta_{ij} \right] J + \delta p \left[ J - J^g \hat{J} - J^g \hat{p} \right] \right] dV - \delta \Pi_{\text{ext}}. \tag{35}$$

Now, by considering the finite element approximations for the solution variables and their variations as,

$$\mathbf{u} = \mathbf{N}_u \mathbf{u}, \quad p = \mathbf{N}_p \mathbf{p}, \tag{36}$$

$$\delta \mathbf{u} = \mathbf{N}_u \delta \mathbf{u}, \quad \delta p = \mathbf{N}_p \delta \mathbf{p}, \tag{37}$$

where,  $\mathbf{u}$  and  $\mathbf{p}$ , respectively, are the nodal degrees of freedom (DOFs) for the displacement and pressure fields, we get the following semi-discrete equilibrium equations,

$$\mathbf{R}_u = \int_{B_i} \mathbf{G}_u^T \hat{\boldsymbol{\sigma}} dV - \mathbf{F}^{\text{ext}} = \mathbf{0}, \tag{38}$$

$$\mathbf{R}_p = \int_{B_0} \mathbf{N}_p^T \left[ J - J^g \hat{J} - J^g \hat{p} \right] dV = \mathbf{0}, \tag{39}$$

where,  $\mathbf{F}^{\text{ext}}$  is the vector of external forces, and it is given by,

$$\mathbf{F}^{\text{ext}} = \int_{B_0} \mathbf{N}_u^T \mathbf{f}_0 J^g dV + \int_{\partial B_0^N} \mathbf{N}_u^T \bar{\mathbf{t}} A^g dA, \tag{40}$$

In Eq. (38),  $\mathbf{G}_u$  is the discrete gradient-displacement matrix. For a single basis function,  $N_u$ ,  $\mathbf{G}_u$  is given as,

$$\mathbf{G}_u = \begin{bmatrix} \frac{\partial N_u}{\partial x} & 0 & 0 & \frac{\partial N_u}{\partial y} & 0 & 0 & \frac{\partial N_u}{\partial z} & 0 & 0 \\ 0 & \frac{\partial N_u}{\partial x} & 0 & 0 & \frac{\partial N_u}{\partial y} & 0 & 0 & \frac{\partial N_u}{\partial z} & 0 \\ 0 & 0 & \frac{\partial N_u}{\partial x} & 0 & 0 & \frac{\partial N_u}{\partial y} & 0 & 0 & \frac{\partial N_u}{\partial z} \end{bmatrix}^T. \tag{41}$$

Following the representation of  $\mathbf{G}_u$  in the matrix form, the Cauchy stress tensor is represented in the vector form as,

$$\hat{\boldsymbol{\sigma}} = \hat{\sigma}_{ij} = [\hat{\sigma}_{xx} \quad \hat{\sigma}_{yx} \quad \hat{\sigma}_{zx} \quad \hat{\sigma}_{xy} \quad \hat{\sigma}_{yy} \quad \hat{\sigma}_{zy} \quad \hat{\sigma}_{xz} \quad \hat{\sigma}_{yz} \quad \hat{\sigma}_{zz}]^T. \tag{42}$$

### 3.1. Newton–Raphson scheme for the coupled system

We solve the coupled nonlinear Eqs. (38) and (39) using an incremental iterative approach in which the growth tensor is applied in a number of load steps. Assuming that the subscripts  $n + 1$  and  $n$  denote the current and previously converged load steps, respectively, the displacement DOFs, pressure DOFs and the growth tensor at the current load step,  $\mathbf{u}_{n+1}$ ,  $\mathbf{p}_{n+1}$  and  $\mathbf{F}_{n+1}^g$  are computed as the load step increments,  $\Delta \mathbf{u}$ ,  $\Delta \mathbf{p}$  and  $\Delta \mathbf{F}^g$ , from the respective quantities at the previously converged load step,  $\mathbf{u}_n$ ,  $\mathbf{p}_n$  and  $\mathbf{F}_n^g$ , as

$$\mathbf{u}_{n+1} = \mathbf{u}_n + \Delta \mathbf{u}, \tag{43}$$

$$\mathbf{p}_{n+1} = \mathbf{p}_n + \Delta \mathbf{p}, \tag{44}$$

$$\mathbf{F}_{n+1}^g = \mathbf{F}_n^g + \Delta \mathbf{F}^g. \tag{45}$$

With  $\Delta \mathbf{F}^g$  as the input, the coupled nonlinear equations (38) and (39) are solved for the load step increments in the degrees of freedom in an iterative manner using the Newton–Raphson scheme. Using the iterative increments  $\bar{\Delta} \mathbf{u}$  and  $\bar{\Delta} \mathbf{p}$ , vectors  $\mathbf{u}_{n+1}$  and  $\mathbf{p}_{n+1}$  at the current iteration  $k + 1$  can be written as,

$$\left. \begin{aligned} \mathbf{u}_{n+1}^{(k+1)} &= \mathbf{u}_n + \Delta \mathbf{u}^{(k+1)} = \mathbf{u}_n + \Delta \mathbf{u}^{(k)} + \bar{\Delta} \mathbf{u} = \mathbf{u}_{n+1}^{(k)} + \bar{\Delta} \mathbf{u}, \\ \mathbf{p}_{n+1}^{(k+1)} &= \mathbf{p}_n + \Delta \mathbf{p}^{(k+1)} = \mathbf{p}_n + \Delta \mathbf{p}^{(k)} + \bar{\Delta} \mathbf{p} = \mathbf{p}_{n+1}^{(k)} + \bar{\Delta} \mathbf{p}, \end{aligned} \right\} \text{for } k = 1, 2, 3, \dots, k_{\text{max}}. \tag{46}$$

where  $k_{\text{max}}$  is the maximum number of iterations.

By adapting the Newton–Raphson scheme, we arrive at the coupled matrix system given as

$$\begin{bmatrix} \mathbf{K}_{uu} & \mathbf{K}_{up} \\ \mathbf{K}_{pu} & \mathbf{K}_{pp} \end{bmatrix} \begin{Bmatrix} \bar{\Delta} \mathbf{u} \\ \bar{\Delta} \mathbf{p} \end{Bmatrix} = - \begin{Bmatrix} \mathbf{R}_u \\ \mathbf{R}_p \end{Bmatrix} \tag{47}$$

where,

$$\mathbf{K}_{uu} = \int_{B_i} \mathbf{G}_u^T \mathbf{e}(u_{n+1}^k, p_{n+1}^k) \mathbf{G}_u \, dV, \quad (48)$$

$$\mathbf{K}_{up} = \int_{B_i} \mathbf{D}_u^T \mathbf{N}_p \, dV = \mathbf{K}_{pu}^T \quad (49)$$

$$\mathbf{K}_{pp} = - \int_{B_0} J_{n+1}^g \hat{\vartheta} \mathbf{N}_p^T \mathbf{N}_p \, dV \quad (50)$$

$$\mathbf{R}_u = \int_{B_i} \mathbf{G}_u^T \hat{\mathbf{G}}(u_{n+1}^k, p_{n+1}^k) \, dV - \mathbf{F}_{n+1}^{\text{ext}}, \quad (51)$$

$$\mathbf{R}_p = \int_{B_0} \mathbf{N}_p^T \left[ J_{n+1}^k - J_{n+1}^g \hat{\mathbf{J}} - J_{n+1}^g \hat{\vartheta} p_{n+1}^k \right] \, dV, \quad (52)$$

where,  $\mathbf{e}$  is the matrix representation of the material tangent tensor  $\mathbf{e}$ , see [Appendix A](#) for the details. In the sub-matrix  $\mathbf{K}_{up}$ ,  $\mathbf{D}_u$  is the divergence–displacement matrix, which, for a single basis function,  $N_u$ , is given as

$$\mathbf{D}_u = \begin{bmatrix} \frac{\partial N_u}{\partial x} & \frac{\partial N_u}{\partial y} & \frac{\partial N_u}{\partial z} \end{bmatrix}. \quad (53)$$

### 3.2. Finite element spaces

In the Q1/P0 element, displacement is discretised with the continuous 4-noded quadrilateral element in 2D and 8-noded hexahedral element in 3D while the pressure is constant within an element. Despite its simplicity and success in modelling (nearly) incompressibility by choosing a high enough value for the bulk modulus to impose the incompressibility condition weakly, the fundamental disadvantage of the Q1/P0 element is its lack of *inf-sup* stability and the need to use finer meshes to obtain accurate results, see [Kadapa and Hossain \(2020b\)](#). To overcome these issues, we employ higher-order elements. The state-of-the-art finite element framework for computational solid mechanics based on the Bézier elements as devised by [Kadapa \(2019a,b\)](#) and [Kadapa and Hossain \(2020b\)](#) is adapted in this work.

We propose five different element shapes that offer flexibility in discretising geometries of varying complexities in size and shape. The element shapes and the corresponding displacement and pressure nodes in each element are depicted in [Fig. 1](#). The triangular and tetrahedral elements are denoted as BT2/BT1; the quadrilateral and hexahedron elements are denoted as BQ2/BQ1; and the wedge element is denoted as BW2/BW1. The *inf-sup* stability of the BQ2/BQ1 and BW2/BW1 elements can be established following a similar technique adapted for the BT2/BT1 element in [Kadapa \(2019b\)](#).

**Remark.** *Inf-sup* stable elements for the displacement–pressure combination based on any appropriate family of elements, for example, Lagrange elements (Taylor–Hood elements [Brezzi and Fortin, 1991](#)), Bézier elements ([Kadapa, 2019b](#)) and NURBS ([Kadapa et al., 2016](#)), are equally suitable for the present mixed formulation. We use the framework based on Bézier elements since it offers several advantages in the simulation of soft and smart materials ([Kadapa, 2019a,b](#); [Kadapa and Hossain, 2020b](#); [Kadapa, 2020](#)). Unlike NURBS, Bézier elements support various element shapes suitable for meshing complex geometries. Besides, because of the non-negative nature of Bernstein polynomials, Bézier elements are amenable for explicit dynamic simulations using lumped-mass matrices, which is not so straightforward in the case of quadratic Lagrange elements, [Kadapa \(2019a,b, 2020\)](#).

#### 3.2.1. Special treatment for pressure DOFs across interfaces

The basis functions considered for pressure field in the present work are such that the pressure is  $C^0$  continuous across element boundaries. Such an approximation, however, fails to accurately capture stress discontinuities at interfaces for problems consisting of multiple layers modelled either with different elastic moduli or growth functions, which is common in models encountered in growth-induced deformation phenomena. To accurately model discontinuities in the stress/pressure field across material interfaces, the pressure DOFs across the material interfaces are duplicated, as illustrated schematically for the case of BQ2/BQ1 element in 2D in [Fig. 2](#). Thus, for problems with multiple layers, the pressure field is continuous within each layer but is discontinuous across interfaces.

## 4. Numerical examples

In this section, several numerical examples are presented to demonstrate the capability of the proposed framework in simulating compressible and incompressible deformation behaviour in soft materials. For the plane-strain problems, the domain is assumed to be in the X–Y plane. The proposed finite element formulation is implemented in an in-house C++ code using third-party libraries Eigen ([Guennebaud et al., 2010](#)) and PARDISO ([Kourounis et al., 2018](#)) for matrix algebra. The finite element meshes used in this work are generated using GMSH ([Geuzaine and Remacle, 2009](#)) and the mapping for quadratic Bézier elements presented in [Kadapa \(2019a\)](#).

Three different constitutive models, namely Neo-Hookean, Gent and Arruda–Boyce models, are used for modelling the elastic deformation behaviour in the present work. The energy functions for these models are given as follows.

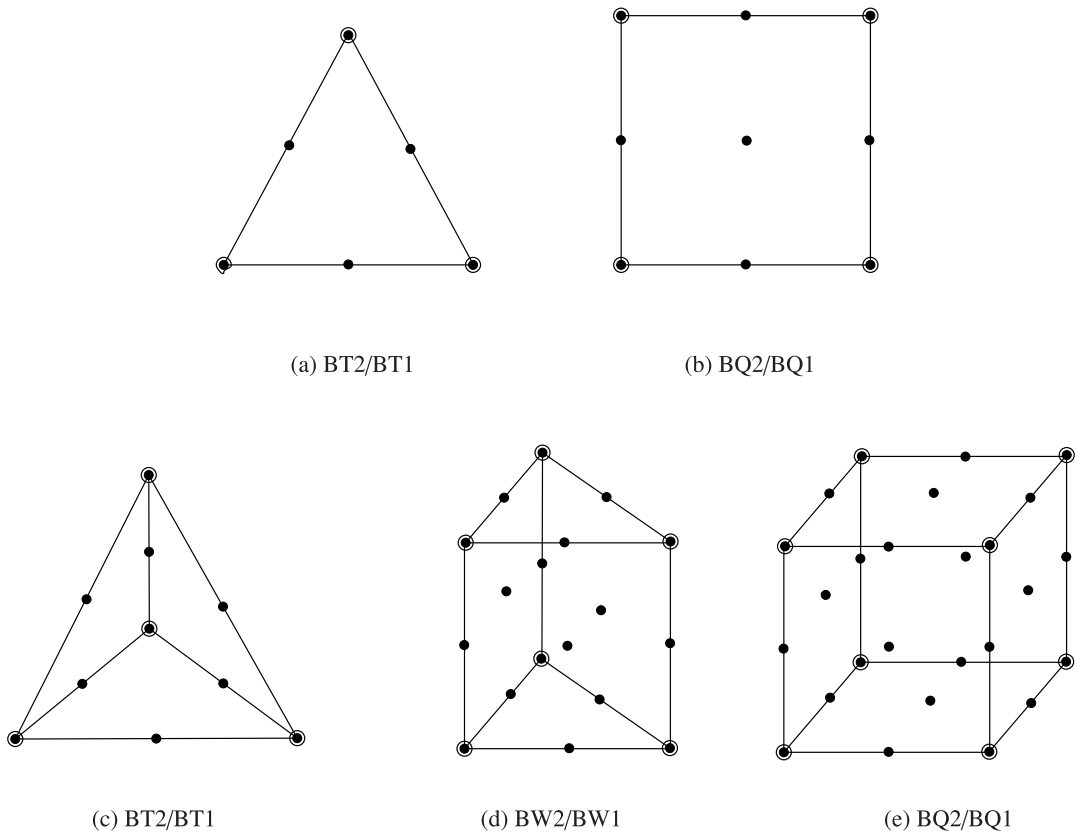


Fig. 1. Different element types considered in this work. Markers • and ○ denote displacement and pressure DOFs, respectively.

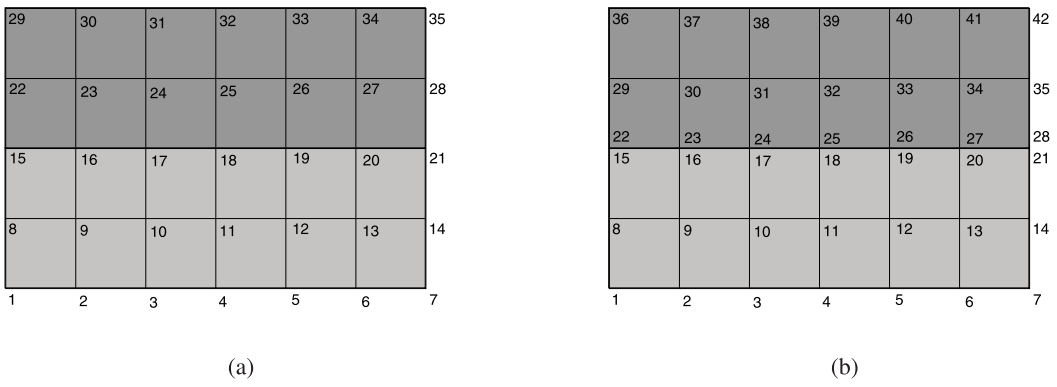


Fig. 2. An example with a material interface: pressure nodes using the BQ2/BQ1 element with (a) continuous approximation and (b) discontinuous approximation for the pressure field. Pressures nodes at the interface between two layers are duplicated to accurately capture the discontinuities.

• Neo-Hookean model:

$$\psi^{dev}(\bar{C}^e) = \frac{\mu}{2} [I_{\bar{C}^e} - 3] \tag{54}$$

• Gent model:

$$\psi^{dev}(\bar{C}^e) = -\frac{\mu I_m}{2} \ln \left( 1 - \frac{I_{\bar{C}^e} - 3}{I_m} \right) \tag{55}$$

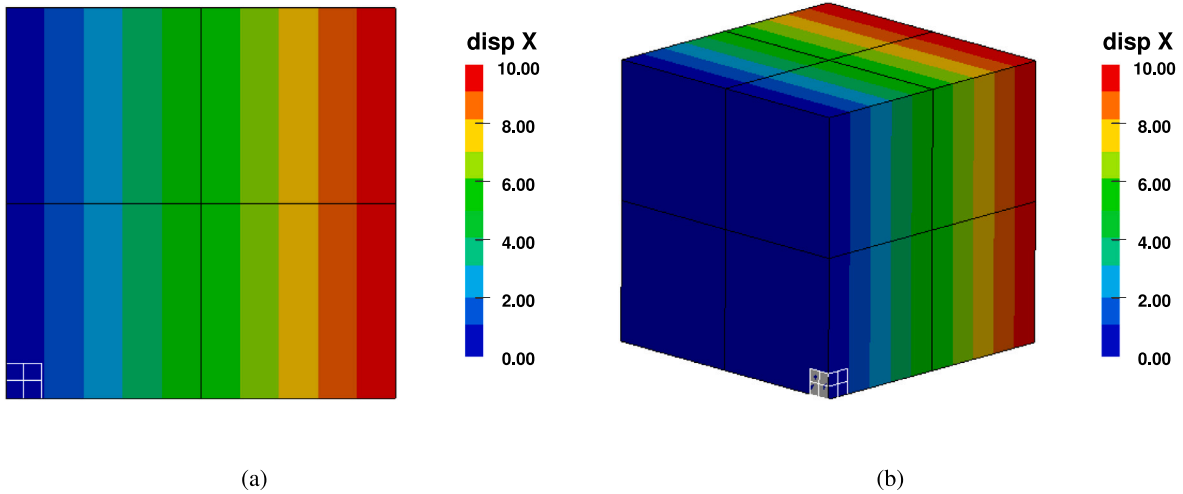


Fig. 3. Block with pure growth: contour plots of X-displacement for (a) plane-strain case and (b) 3D case.

• Arruda–Boyce model:

$$\begin{aligned} \psi^{\text{dev}}(\bar{\mathbf{C}}^e) &= \frac{\mu}{2} \left[ I_{\bar{\mathbf{C}}^e} - 3 \right] + \frac{\mu}{20N} \left[ I_{\bar{\mathbf{C}}^e}^2 - 3^2 \right] \\ &+ \frac{11\mu}{1050N^2} \left[ I_{\bar{\mathbf{C}}^e}^3 - 3^3 \right] + \frac{19\mu}{7000N^3} \left[ I_{\bar{\mathbf{C}}^e}^4 - 3^4 \right] + \frac{519\mu}{673750N^4} \left[ I_{\bar{\mathbf{C}}^e}^5 - 3^5 \right] \end{aligned} \quad (56)$$

where,  $\mu$  is the shear modulus,  $I_{\bar{\mathbf{C}}^e} = \text{tr}(\bar{\mathbf{C}}^e)$ ,  $I_m$  is a material parameter, and  $N$  is the measure of cross-link density of polymers. The volumetric energy function ( $\psi^{\text{vol}}$ ) considered in the present work is

$$\psi^{\text{vol}}(J^e) = \frac{\kappa}{2} [J^e - 1]^2, \quad (57)$$

where,  $\kappa$  is the bulk modulus.

If not specified explicitly, all the values for geometric and material parameters considered in the numerical examples are dimensionless. The shear modulus is  $\mu = 1000$  and the Poisson’s ratio is  $\nu = 0.5$ , unless stated otherwise, for the higher-order elements. Since the Q1/P0 element is invalid for the truly incompressible case, the incompressibility constraint is enforced weakly by choosing a large value for the bulk modulus, see Reese and Govindjee (1998). In this work, we assume  $\kappa=10^4 \mu$  for the simulations with the Q1/P0 element.

#### 4.1. Block with pure volumetric growth

As the first example, we consider a block of unit side length in plane-strain and 3D to demonstrate the effectiveness of the proposed scheme in capturing pure volumetric growth. The finite element mesh consists of  $2 \times 2$  and  $2 \times 2 \times 2$  BQ2/BQ1 elements, respectively, in plane-strain (2D) and 3D. The results obtained with the other elements are indistinguishable from those of the BQ2/BQ1 element; therefore, they are not presented for this example for the sake of clarity. The growth tensor  $\mathbf{F}^g$  is assumed as,

$$\mathbf{F}^g = \begin{bmatrix} 11 & 0 & 0 \\ 0 & 11 & 0 \\ 0 & 0 & 1 \end{bmatrix} \text{ for plane-strain; } \quad \mathbf{F}^g = \begin{bmatrix} 11 & 0 & 0 \\ 0 & 11 & 0 \\ 0 & 0 & 11 \end{bmatrix} \text{ for 3D,} \quad (58)$$

such that the block stretches by a factor of 11 in each allowed coordinate direction, resulting in final configurations that are 121 and 1331 times their original volumes, respectively, in plane-strain and 3D. Fig. 3 shows the contour plots of X-displacement for both the cases. As shown, the proposed scheme yields accurate results for the displacement field. Moreover, the contour plots of nodal pressure presented in Fig. 4 illustrate that pressure field obtained with the proposed scheme is zero (within machine precision) throughout the domain; this is a manifestation of the stress-free final configurations due to pure volumetric growth.

#### 4.2. Single-layer plate in plane-strain

In this example, we establish the spatial convergence properties of the proposed finite element framework using the example of a single-layer plate assuming plane-strain condition. This example is recently studied extensively using analytical methods in Wang et al. (2018b). The initial domain of the plate, as shown in Fig. 5, is  $[-1, 1] \times [0, 0.1]$ . The growth tensor  $\mathbf{F}^g$  is assumed as,

$$\mathbf{F}^g = \begin{bmatrix} 1 + \pi Y & 0 & 0 \\ 0 & 1 & 0 \\ 0 & 0 & 1 \end{bmatrix} \quad (59)$$

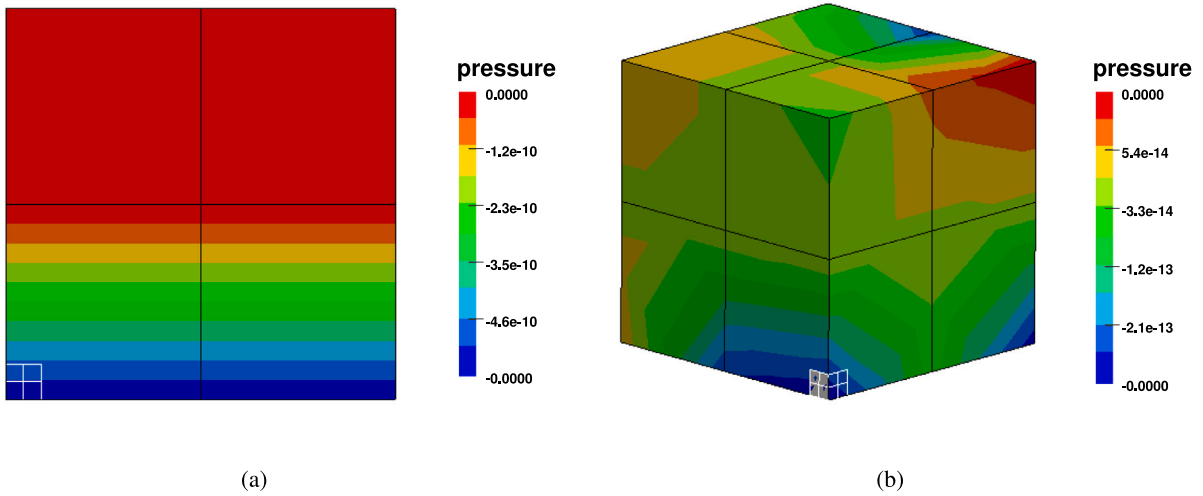


Fig. 4. Block with pure growth: contour plots of nodal pressure for (a) plane-strain case and (b) 3D case.

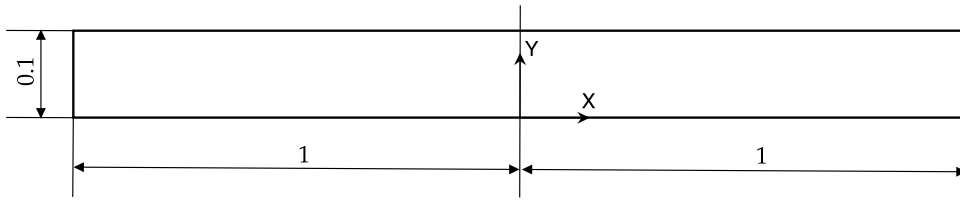


Fig. 5. A single-layer plate in plane-strain condition: geometry of the problem. The drawing is not to scale.

Following Wang et al. (2018b), the analytical solution for the problem is

$$x = r \sin(\pi X), \quad y = r \cos(\pi X) - \frac{1}{\pi}, \quad p = 0, \quad \text{with} \quad r = Y + \frac{1}{\pi}. \tag{60}$$

Due to the symmetry of geometry and loading conditions, only half a portion of the plate is considered for the analysis. The edge at  $X = 0$  is constrained in X-direction, and the node at  $X = Y = 0$  is fixed in Y-direction. The setup of the problem is such that the plate undergoes stress-free deformation due to the induced growth. As a consequence, the hydrostatic pressure is zero throughout the domain of the plate.

Starting with a  $10 \times 2$  mesh for the BQ2/BQ1 and Q1/P0 elements, and a  $(10 \times 2) \times 2$  mesh for the BT2/BT1 element, numerical results are computed for four successively refined meshes. The accuracy of the results is presented in the form of error norms in the displacement and pressure field for all three elements in Fig. 6. It can be observed from the graphs of error norms that while theoretical convergence rates are obtained for the Q1/P0 element, the convergence rates for the BQ2/BQ1 and BT2/BT1 elements are higher than the theoretical convergence rates of three and two, respectively, for displacement and pressure. The superior accuracy of the BQ2/BQ1 and BT2/BT1 elements manifests in the accurate capturing of the bending behaviour using very coarse meshes, as shown in Fig. 7, as opposed to the need for finer meshes in the case of Q1/P0 element, see Fig. 8. The BQ2/BQ1 element with the  $10 \times 2$  mesh, which consists of only 105 nodes produces superior quality results than the Q1/P0 element with  $80 \times 16$  mesh consisting of 1377 nodes. The ability to compute accurate numerical using very coarse meshes by the proposed mixed elements yields significant computational benefits for 3D problems, as demonstrated in the following examples.

### 4.3. Multi-layer plate in plane-strain

We present the accuracy of the higher-order elements as well as the effectiveness of the strategy of duplicating pressure nodes at the interfaces using the example of multi-layered plate in plane-strain condition. The plate occupies the domain  $[-1, 1] \times [-0.0875, 0.0125]$  in the original configuration and it is assumed to be made of four layers with the thickness of each layer being 0.025 units, see Fig. 9. The analysis is performed using only half of the domain and with the same boundary conditions as in the previous example. The growth tensor is assumed as,

$$F^g = \begin{bmatrix} \lambda_1 & 0 & 0 \\ 0 & 1 & 0 \\ 0 & 0 & 1 \end{bmatrix}, \tag{61}$$

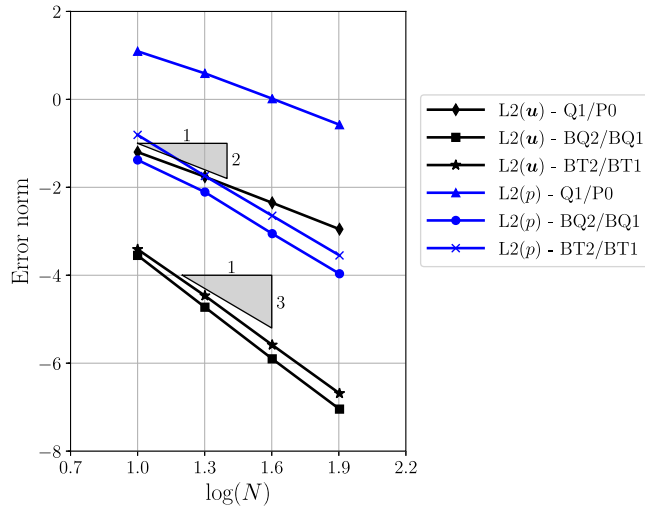


Fig. 6. A single-layer plate in plane-strain condition: convergence of error norms with respect to mesh refinement for the Q1/P0, BT2/BT1 and BQ2/BQ1 elements.  $N$  is the number of elements across the thickness of the plate.

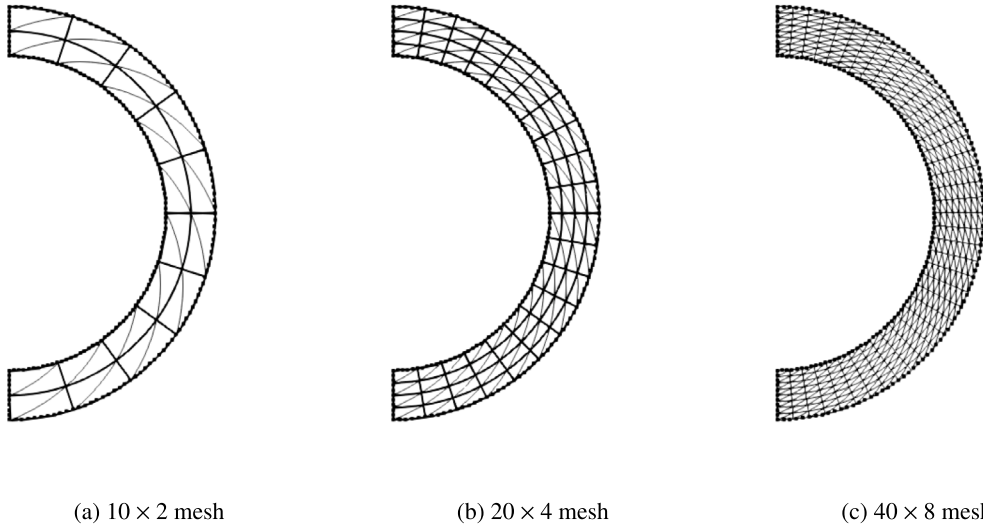


Fig. 7. A single-layer plate in plane-strain condition: comparison of the results obtained with the BQ2/BQ1 element (thick lines) and the BT2/BT1 element (thin lines) against the analytical solution (dots).

where,

$$\lambda_1 = 1.1 + \frac{\pi}{80} \quad \text{for the first layer,} \tag{62}$$

$$\lambda_1 = 1.1 + \frac{3\pi}{80} \quad \text{for the second layer,} \tag{63}$$

$$\lambda_1 = 1.1 + \frac{5\pi}{80} \quad \text{for the third layer,} \tag{64}$$

$$\lambda_1 = 1.1 + \frac{7\pi}{80} \quad \text{for the fourth layer.} \tag{65}$$

The analytical solution for this example is given in [Appendix B](#).

BQ2/BQ1 and BT2/BT1 elements produce indistinguishable results. Therefore, the BT2/BT1 element is omitted from the rest of the discussions. For the discretisations with the same number of nodes, the numerical results obtained with the BQ2/BQ1 element outperform those of the Q1/P0 element, as shown in [Fig. 10](#). To get accurate results using the Q1/P0 element, further finer meshes are required; thereby, increasing the computational cost. The effectiveness of the technique employed for capturing stress discontinuous at interfaces discussed in [Section 3.2.1](#) is demonstrated using element-wise contour plots of pressure in [Fig. 11](#).

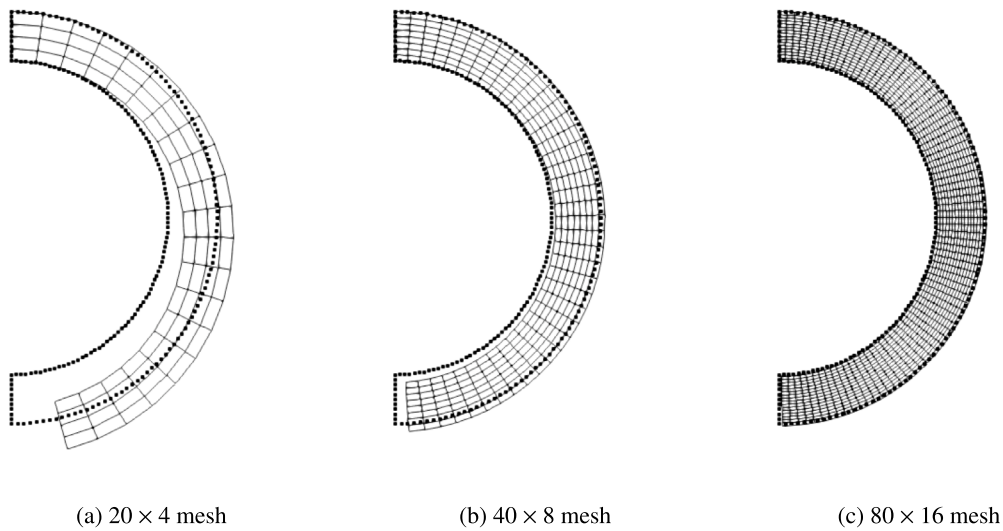


Fig. 8. A single-layer plate in plane-strain condition: comparison of the results obtained with the Q1/P0 element (lines) against the analytical solution (dots).

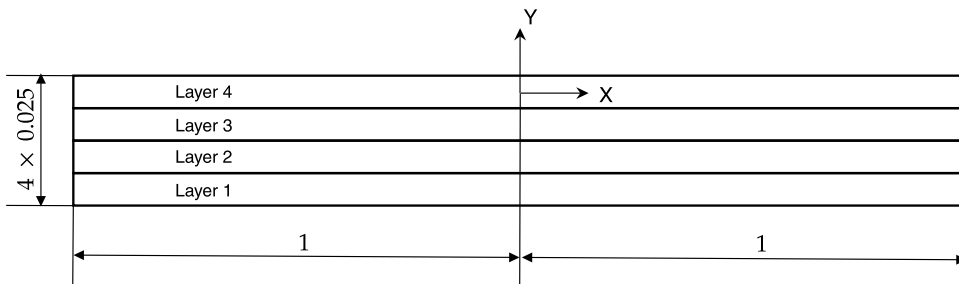


Fig. 9. A four-layered plate in plane-strain condition: geometry of the problem. The drawing is not to scale.

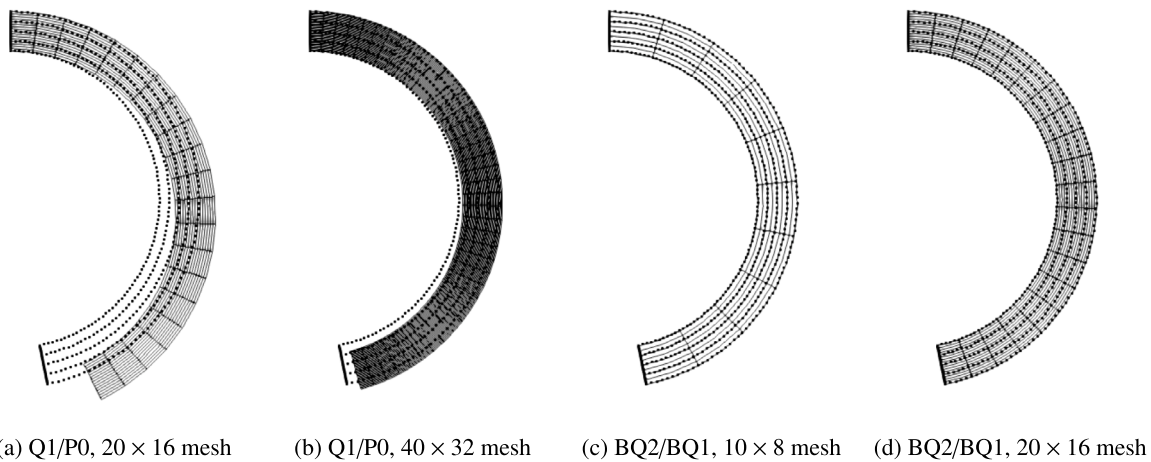


Fig. 10. A four-layered plate in plane-strain: comparison of final deformed configurations obtained with the BQ2/BQ1 and Q1/P0 elements (lines) against the analytical solution (dots).

#### 4.4. Single-layer plate undergoing substantial deformation

This example concerns with substantial growth-induced deformations resulting in what is referred to as a butterfly shape, see Wang et al. (2019). Due to the induced growth, the initially straight plate morphs into a butterfly shape, as depicted in Fig. 12.

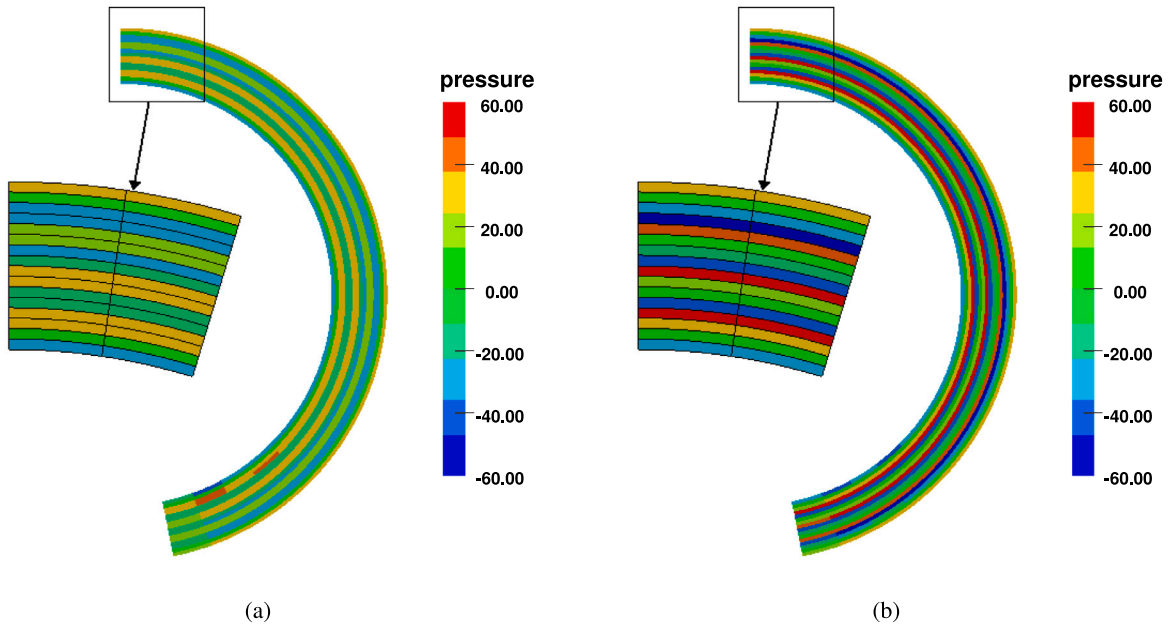


Fig. 11. A four-layered plate in plane-strain: contour plot of element-wise pressure using the BQ2/BQ1 element using (a) without duplicate pressure DOFs and (b) with duplicate pressure DOFs.

The plate occupies the domain  $[-1, 1] \times [0, 0.04]$  in the initial configuration. For the three-dimensional case, the length in the normal direction is assumed to be 0.2 units, and the Dirichlet boundary condition  $u_z = 0$  is applied on the faces  $Z = 0$  and  $Z = 0.2$ . Due to the nature of extremely large deformations, this problem serves as an excellent example to demonstrate the advantages of the proposed computational framework for modelling growth-induced deformation behaviour in soft materials. For the effective presentation of the results, only half of the plate in the positive X-direction is considered for the analysis.

The growth tensor is assumed as,

$$F^g = \begin{bmatrix} \lambda_1 & 0 & 0 \\ 0 & 1 & 0 \\ 0 & 0 & 1 \end{bmatrix}, \tag{66}$$

where,

$$\lambda_1 = \frac{\pi}{2} \sqrt{\cos(\pi X)^2 + 4 \cos(2\pi X)^2} + Y \frac{2\pi [3 \sin(\pi X) + \sin(3\pi X)]}{5 + \cos(2\pi X) + 4 \cos(4\pi X)}. \tag{67}$$

The analytical solution for this example is given in Appendix B.

The final deformed configurations obtained with three different discretisations by the BQ2/BQ1 element are shown in Fig. 13, and the deformed shapes obtained with the Q1/P0 element are shown in Fig. 14. Minor differences still exist in the final deformed shape obtained with the Q1/P0 element with the  $400 \times 16$  mesh. Despite having 16 times more nodes, the Q1/P0 element with  $400 \times 16$  mesh fails to produce accurate results while the BQ2/BQ1 element with the  $50 \times 2$  mesh produces results that match well with the analytical solution. Thus, accurate numerical results can be obtained with coarse meshes using the BQ2/BQ1 element when compared with the Q1/P0 element. This behaviour of higher-order elements also extends the three-dimensional problems, as illustrated in Fig. 15. The wedge and tetrahedral elements offer support for generating meshes for complex geometries usually encountered in real-world applications. Thus, with different element shapes that support mesh generation for simple as well as complex geometries, the proposed framework offers an accurate, flexible, and computationally efficient simulation framework for large-scale three-dimensional problems in morphoelasticity.

#### 4.5. Post-buckling instabilities in bilayer plates

In the last example of this section, we apply the proposed framework for the simulation of post-buckling instabilities in a bilayer plate in plane-strain condition. Adapted from Dortdivanlioglu et al. (2017), the geometry and boundary conditions of the problem are as shown in Fig. 16. Truly incompressible Neo-Hookean model is considered with the ratio of shear moduli for the film and substrate as  $\mu_f/\mu_s = 100$ . The growth tensor is assumed as,

$$F^g = \begin{bmatrix} 1 + g & 0 & 0 \\ 0 & 1 + g & 0 \\ 0 & 0 & 1 \end{bmatrix}, \tag{68}$$

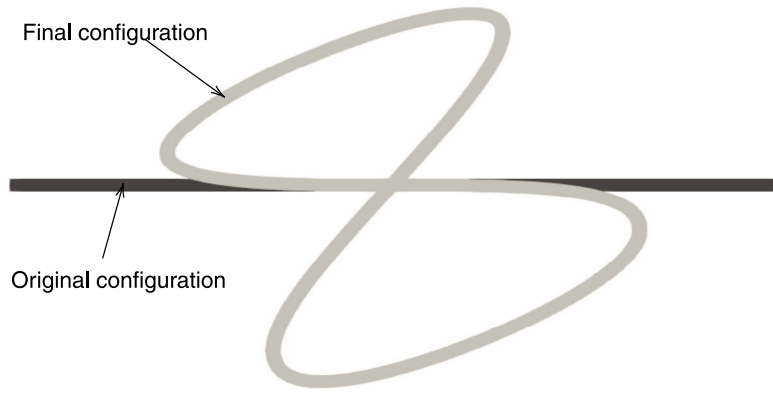


Fig. 12. A single-layer plate with butterfly shape: initial and final configurations.

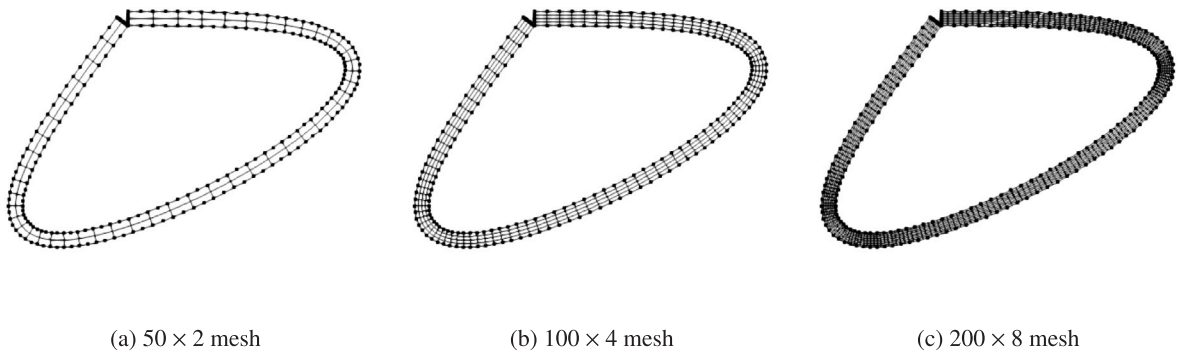


Fig. 13. A single-layer plate with butterfly shape: comparison of final deformed configurations obtained with the BQ2/BQ1 element (mesh lines) against the analytical solution (dots).

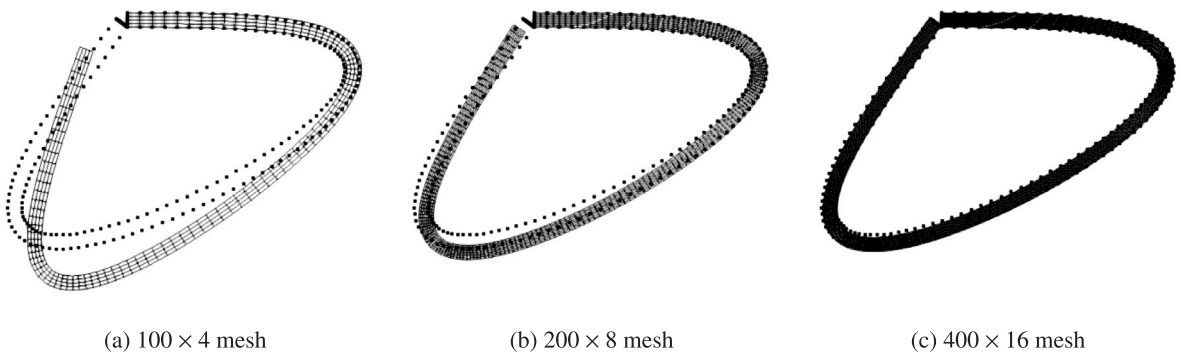


Fig. 14. A single-layer plate with butterfly shape: comparison of final deformed configurations obtained with the Q1/P0 element (mesh lines) against the analytical solution (dots).

where  $g$  is the growth parameter. The finite element mesh consists of  $300 \times 54$  BQ2/BQ1 elements. To trigger the formation of instabilities, a small perturbation is applied to one of the nodes on the top edge of the film. The simulation is carried out by increasing the value of  $g$  in uniform increments of 0.002 until the simulation crashes. The transition from wrinkles to periodic-doubling occurs at  $g = 0.234$ . The evolution of instabilities in the bilayer model is presented in Fig. 17 for four different values of  $g$ . As shown, the proposed framework is capable of predicting the transition from wrinkling to period-doubling without the need for selectively changing the size of domains. Moreover, the contour plots of element-wise pressure in Fig. 18 show that the proposed methodology accurately captures the discontinuity in pressure across the interface between the substrate and the film.

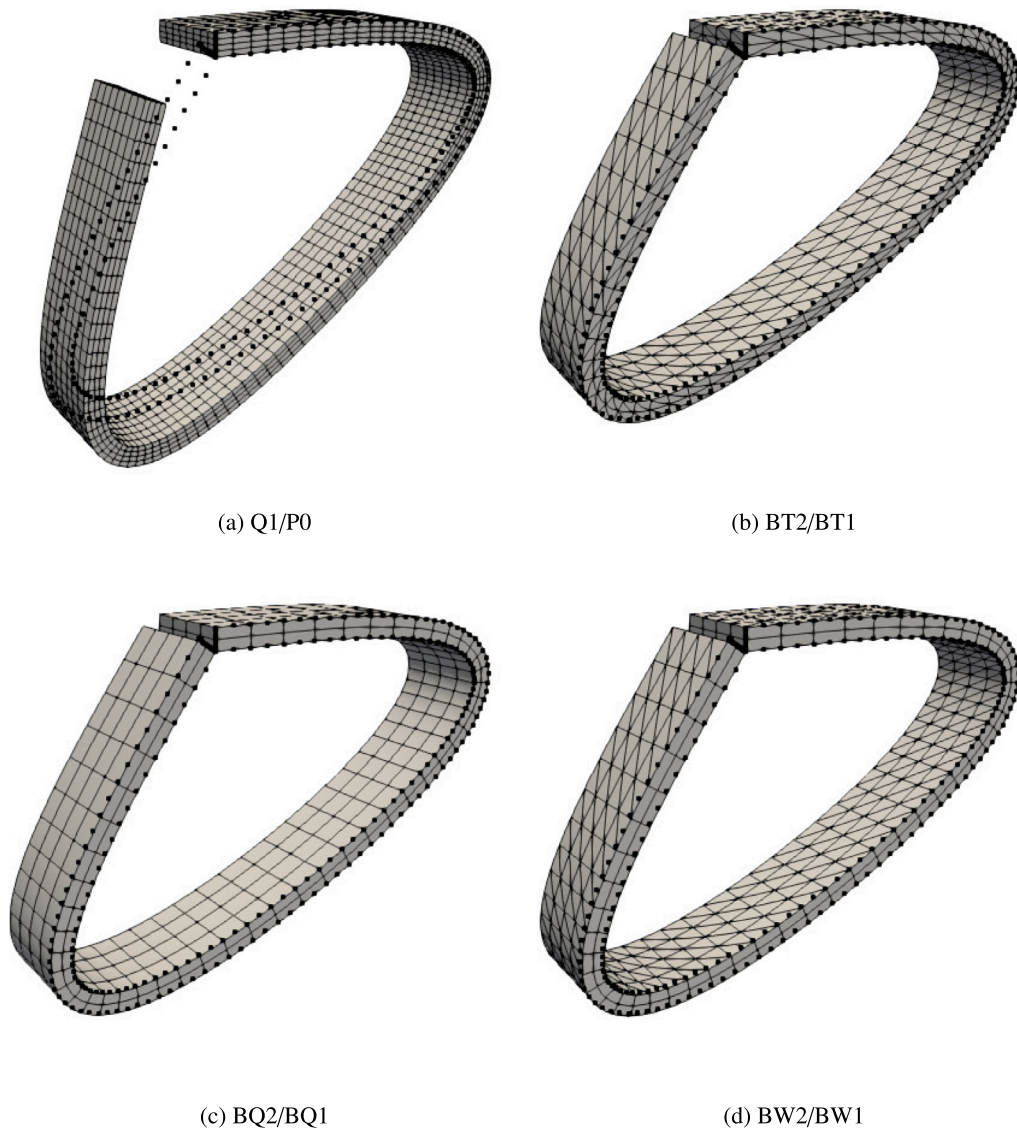


Fig. 15. A single-layer plate with butterfly shape: comparison of final deformed configurations in 3D obtained with the different element types against the analytical solution (dots).

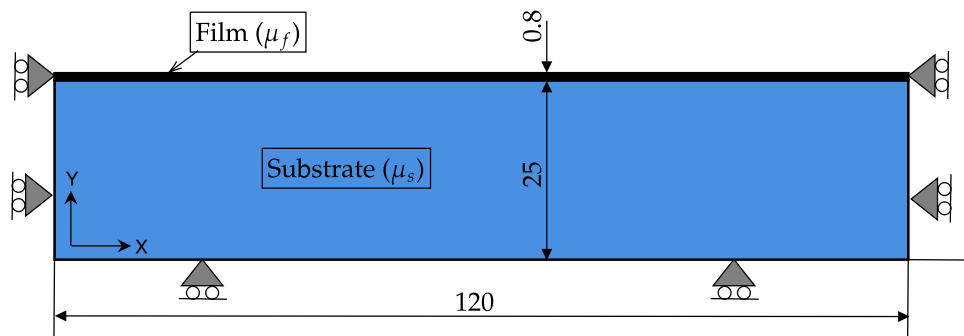


Fig. 16. A bilayer plate: geometry and boundary conditions.

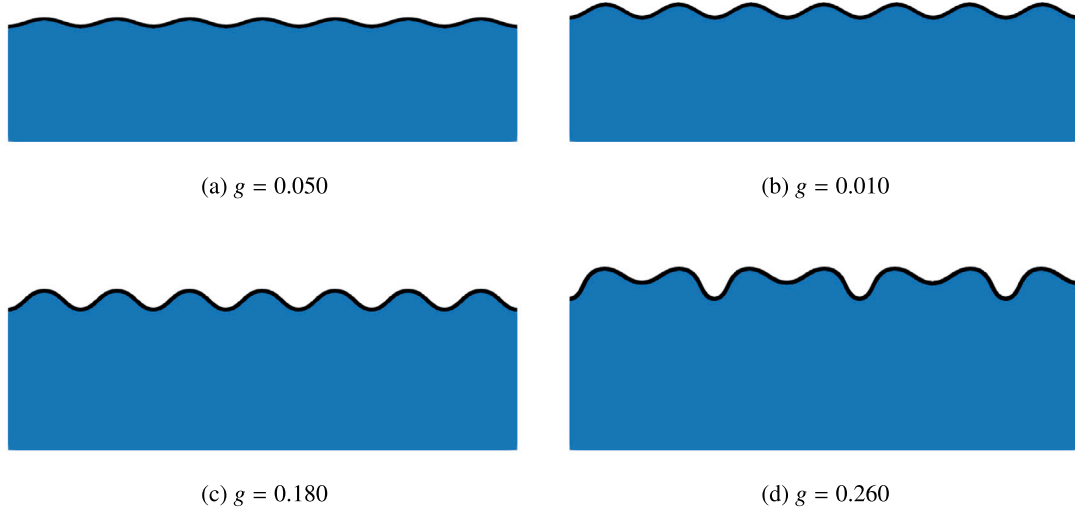


Fig. 17. A bilayer plate: deformed shapes at four different values of the growth parameter.

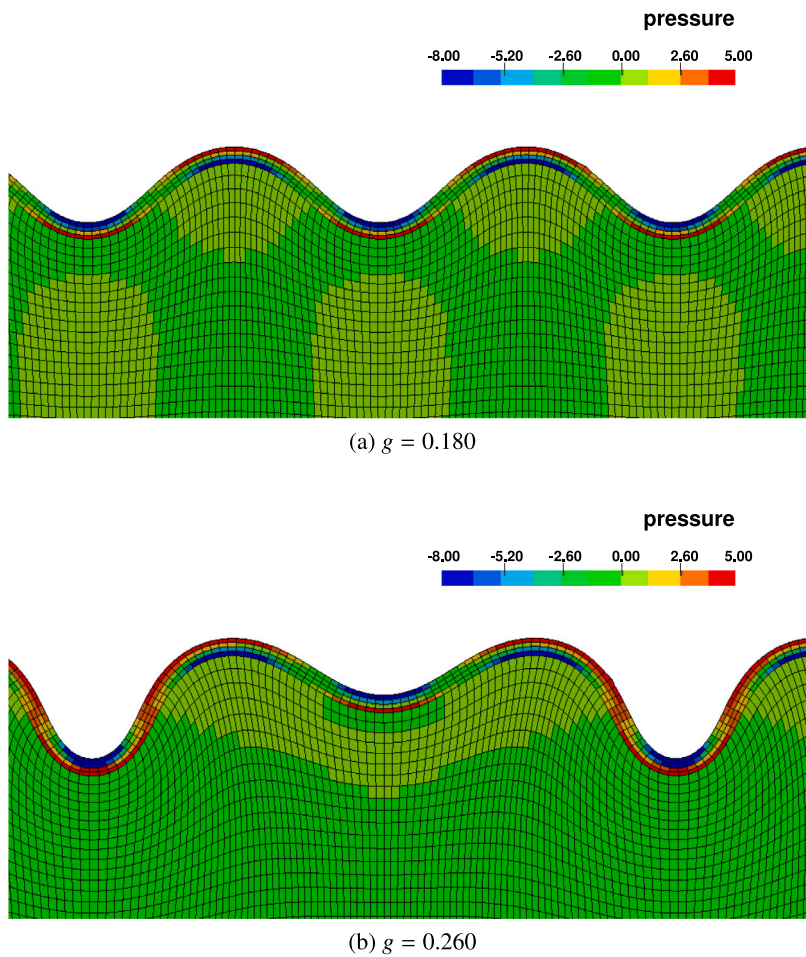


Fig. 18. A bilayer plate: contour plots of element-wise pressure at two different values of the growth parameter.

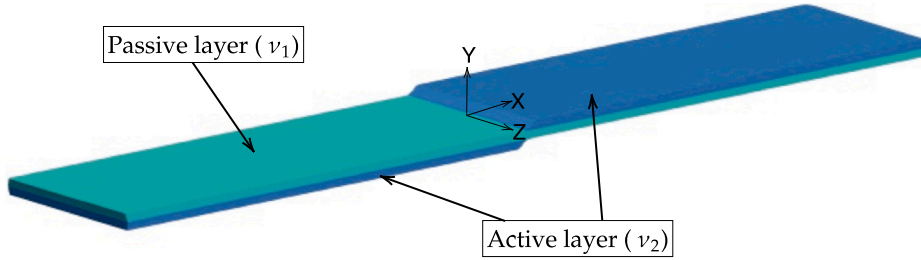


Fig. 19. A bi-layer beam: location of the passive and active layers. The parameters in the brackets represent Poisson’s ratio of the corresponding layer.

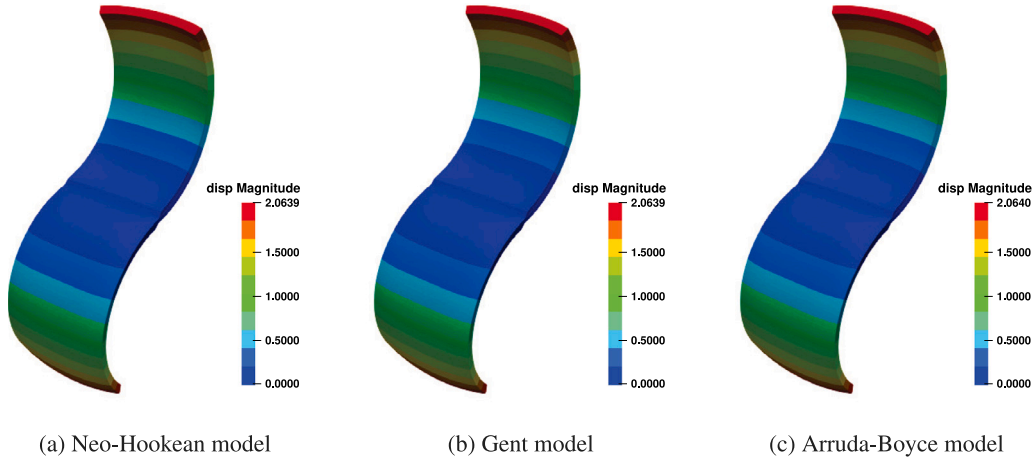


Fig. 20. A bi-layer beam: comparison of deformed shapes obtained with different constitutive models for Poisson’s ratio of  $\nu_1 = \nu_2 = 0.5$ . The material parameter  $I_m$  for the Gent model is 100. The value of cross-link density of polymers  $N$  in the Arruda–Boyce model is 2.8.

5. Effects of compressibility and constitutive models

In this section, we study the effects of different constitutive models and compressibility on the deformations induced by growth or atrophy. It is worth highlighting at this point that this example also serves to demonstrate the capability of the proposed mixed formulation in modelling compressible as well as truly incompressible models in a single problem.

For the demonstration, a bi-layer beam made of polydimethylsiloxane (PDMS) polymer as illustrated by Egunov et al. (2016) is considered. The model consists of two layers, as shown in Fig. 19. The passive layer is of length 4 cm, width 1 cm and thickness 0.02 cm, and each active layer is of length 2 cm. The Young’s modulus is assumed to be 1 MPa. For the purpose of comparison, Neo-Hookean, Gent, and Arruda–Boyce models, and different values of Poisson’s ratio in the range [0.1, 0.5] are considered. Only half of the domain with the symmetric boundary condition in Z-direction is considered for the simulation. The finite element mesh consists of 4977 nodes and 480 BQ2/BQ1 elements. Nodes at  $X = 0$  are fixed in the three coordinate directions, and the rest of the faces are assumed to be traction-free. The growth tensor is assumed to be isotropic.

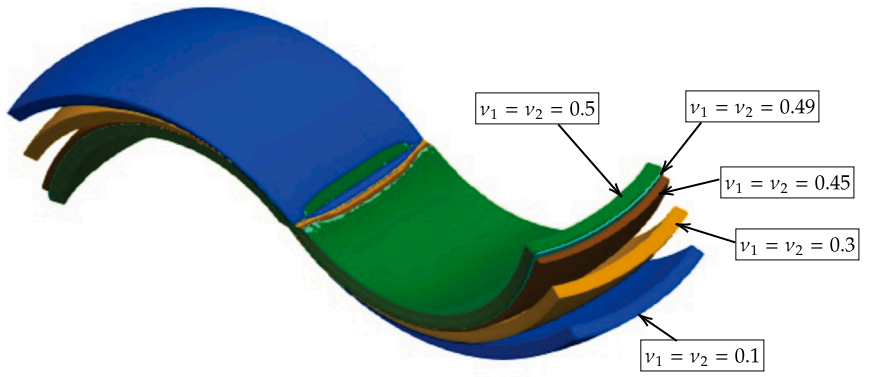
Deformed shapes of the beam obtained with Neo-Hooke, Gent and Arruda–Boyce model for  $g = -0.05$  as shown in Fig. 20, indicate no apparent differences in the results due to the particular choice of constitutive models. However, compressibility has a significant effect on the extent of deformation of the beam, as illustrated in Fig. 21. From the results presented in Fig. 21, we can observe that the deformation of the beam is reduced when one or both the layers are compressible. This behaviour is expected: when the material is compressible, it has more tendency to accommodate volumetric changes than to undergo bending.

6. 3D examples inspired from nature

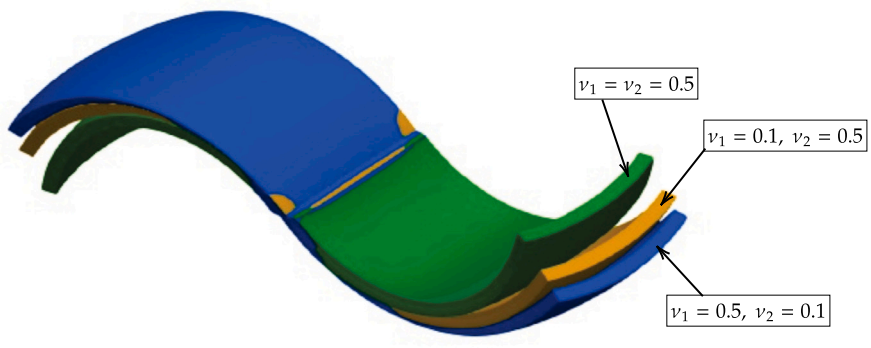
In this section, we demonstrate the potential of the proposed framework for simulating complex growth-induced deformation using three problems observed in nature.

6.1. Morphoelastic rods

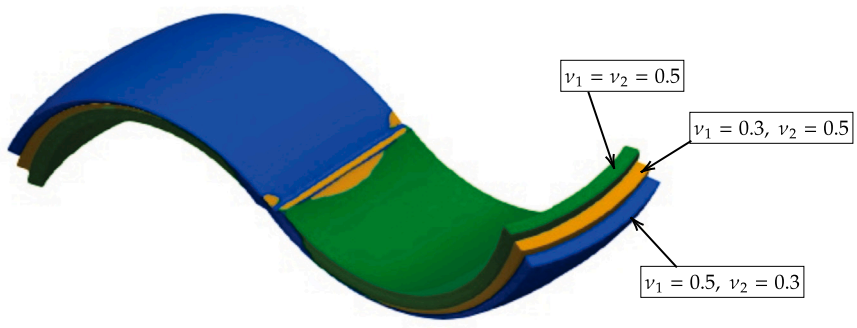
Inspired by the works of Moulton et al. (2013, 2020) and Lessinnes et al. (2017) on morphoelasticity, in this example, we present thin circular hyperelastic rods morphing into various configurations. The radius of the circle is 0.025 units and the length of the



(a)



(b)



(c)

Fig. 21. A bi-layer beam: comparison of deformed shapes obtained with the Neo-Hookean model and different values of Poisson's ratio for the passive and active layers.

rod is four units. Truly incompressible Neo-Hookean hyperelastic model is considered. The initially straight rod is clamped on its face at  $Z = 0$ , and the rest of the faces are assumed to be traction-free. The original configuration of the rod, along with the mesh employed, is shown in Fig. 22a. The finite element mesh consists of 11457 nodes and 1200 BQ2/BQ1 elements. Different growth

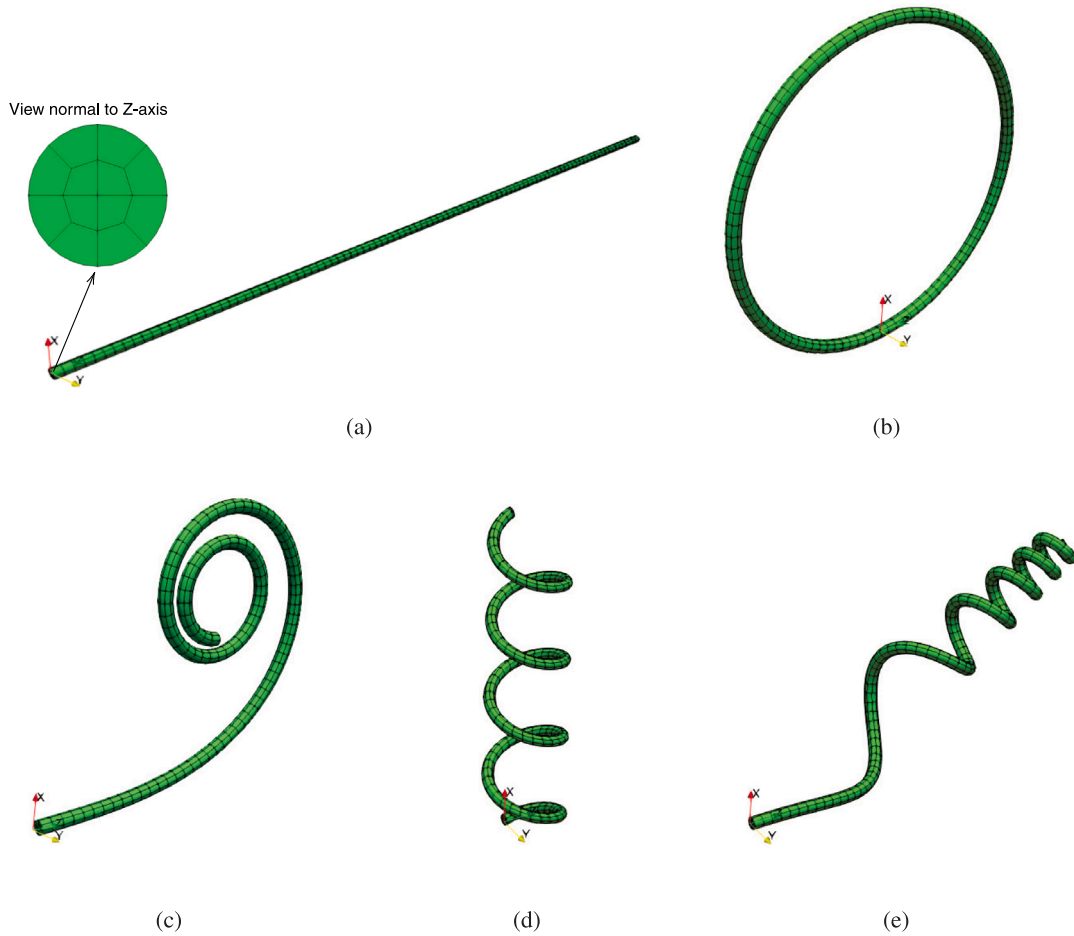


Fig. 22. A morphoelastic rod: (a) original mesh, (b) circular shape with  $F_{11}^g = F_{22}^g = 1, F_{33}^g = 1 - \frac{\pi}{2} X$ ; (c) spiral shape with  $F_{11}^g = F_{22}^g = 1, F_{33}^g = 1 - \frac{\pi}{2} X Z$ ; (d) helical shape with  $F_{11}^g = F_{22}^g = 1, F_{33}^g = 1 - 2\pi Y, F_{13}^g = 0.4$ ; and (e) helical shape with  $F_{11}^g = F_{22}^g = 1, F_{33}^g = 1 + 4 Z [X \cos(\pi Z) + Y \sin(\pi Z)]$ .

tensors resulting in circular, spiral, and helical shapes are considered. Shape morphing of the circular rod into four different final configurations for the assumed growth tensors is shown in Fig. 22.

### 6.2. Flower petals

Inspired by the growth-induced deformation in flower petals and hydrogel-based robotics, in this example, we simulate the morphoelastic deformation of a flower with four petals. The setup of the problem is akin to the example presented in Wang et al. (2020). The initial configuration is as shown in Fig. 23. The length of each arm is two units. The petals are assumed to be made of two layers with the thickness of the bottom and top layers being 0.02 and 0.03 units, respectively. The bottom layer is the active layer, and the top layer is passive, meaning that the growth tensor is applied only in the bottom layer. The shear moduli of the bottom and top layers are 1000 and 10 000 units, respectively. Due to the symmetry, only a quarter of the model discretised with wedge elements is considered for the simulation. The finite element mesh consists of 8767 nodes and 1790 BW2/BW1 elements.

Two different growth tensors are considered for the simulations: (i) isotropic case with growth in all coordinate directions and (ii) anisotropic case with atrophy in X-direction and growth in Y- and Z-directions. Simulations are performed using an increment/decrement of 0.001. In the case of isotropic growth, the petals bend upwards (in the positive Z-direction) and deform into a closed position, as illustrated in Fig. 24. However, in the case of anisotropic growth, two of the petals oriented along the Y-axis bend upwards and the other two which are oriented along the X-axis bend downwards, as shown in Fig. 25. The downward-bending petals can be considered to mimic the behaviour of dying petals. It can be observed from this example that, for the same value of growth parameter, the magnitude of bending deformation of the petals oriented towards Y-axis decreases substantially from the case with isotropic growth tensor to the one with anisotropic growth tensor.

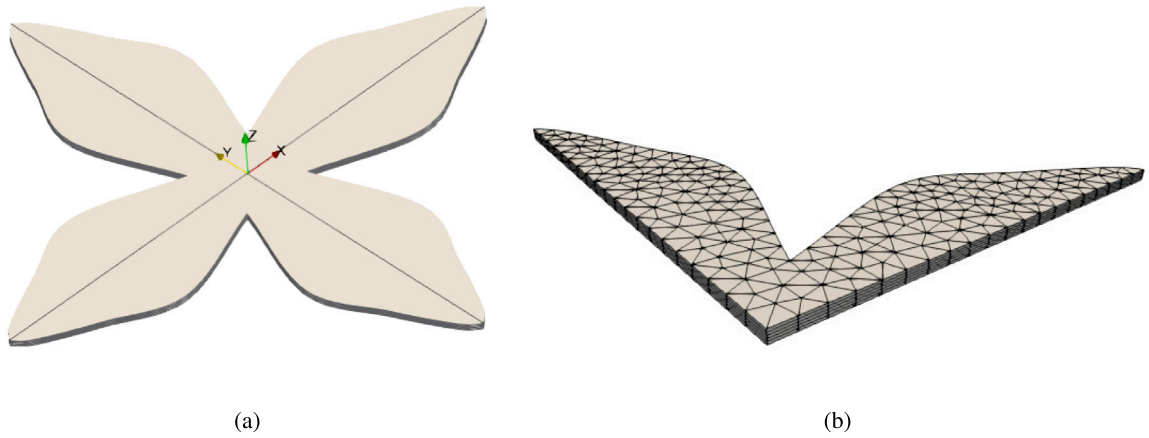


Fig. 23. Lily petals: (a) original configuration of lily with four petals and (b) finite element mesh.

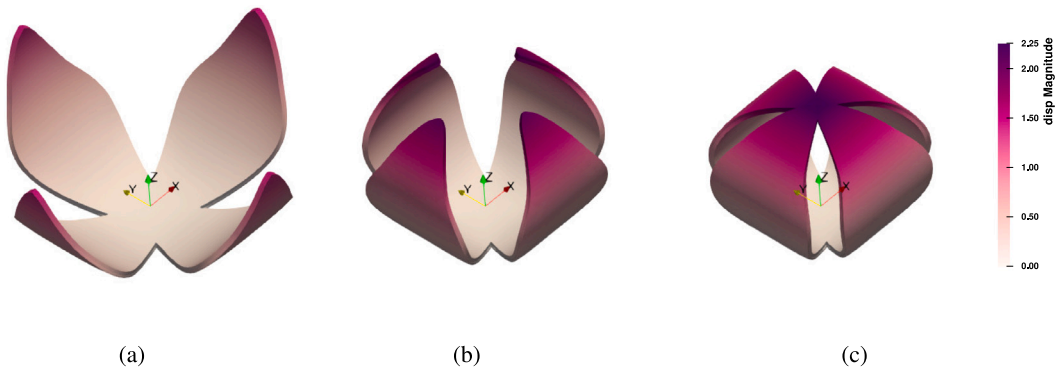


Fig. 24. Lily petals: deformed configurations at (a)  $F_{11}^g = F_{22}^g = F_{33}^g = 1.05$ , (b)  $F_{11}^g = F_{22}^g = F_{33}^g = 1.075$  and (c)  $F_{11}^g = F_{22}^g = F_{33}^g = 1.09$ . These values correspond to 50th, 75th and 90th load steps of the simulation.

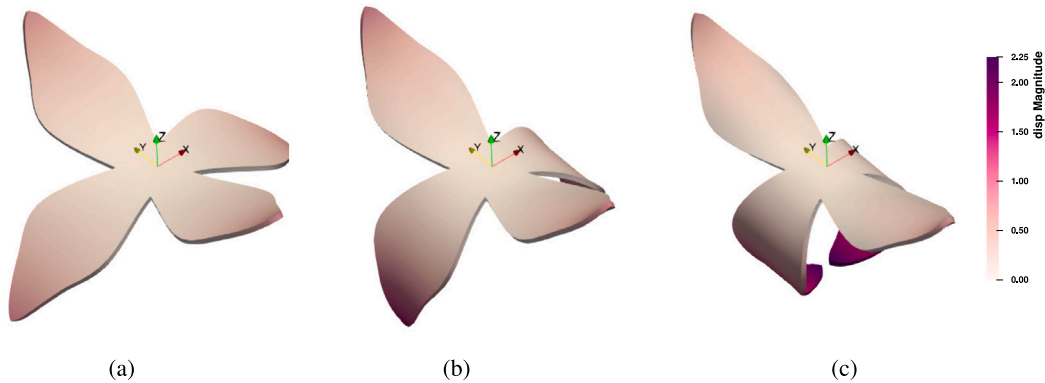


Fig. 25. Lily petals: deformed configurations at (a)  $F_{11}^g = 0.95, F_{22}^g = F_{33}^g = 1.05$ , (b)  $F_{11}^g = 0.9, F_{22}^g = F_{33}^g = 1.1$  and (c)  $F_{11}^g = 0.85, F_{22}^g = F_{33}^g = 1.15$ . These values correspond to 50th, 100th and 150th load steps of the simulation.

### 6.3. Thin tubular section

As the last example, growth-induced deformations in a thin cylindrical tube is considered. The outer diameter of the tube is one unit, its thickness 0.02 units and the length is two units. Only a quarter portion of the tube is modelled using a finite element mesh consists of 7749 nodes and 800 BQ2/BQ1 elements. Fig. 26 shows the original shape of the tube and its deformed shapes under three different growth tensors. Note that the deformed shapes presented are not in the post-buckling regime but are those obtained

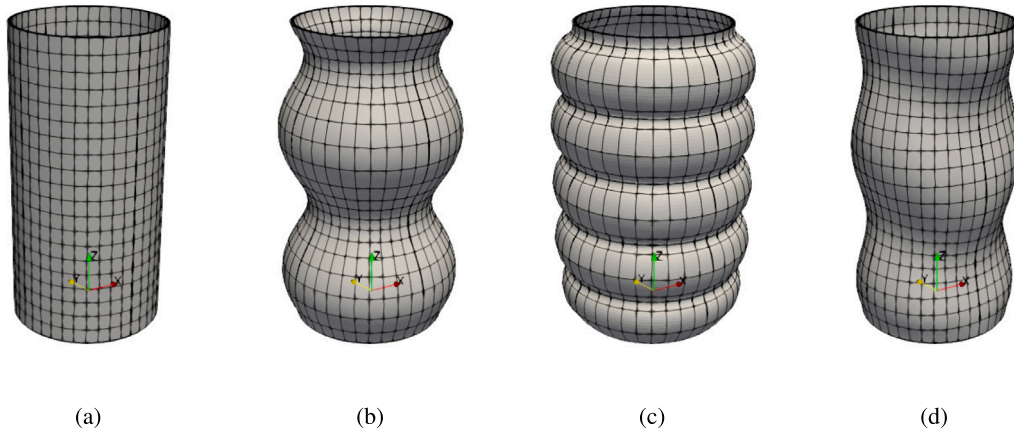


Fig. 26. Morphoelastic tubes: fixed-fixed tube (a) original shape, (b) deformed shape with  $F_{11}^g = F_{22}^g = F_{33}^g = 1 + 0.3 \sin(2\pi Z)$ , (c) deformed shape with  $F_{11}^g = F_{22}^g = F_{33}^g = 1 + 0.6 \sin(5\pi Z)$ , and (d) deformed shape with  $F_{11}^g = F_{22}^g = F_{33}^g = 1 + 0.2 [X \sin(2\pi Z) + Y \cos(2\pi Z)]$ .

by selectively adjusting the growth tensor using trigonometric functions. Thus, the proposed work offers an efficient numerical framework for performing quick simulations of complex growth-induced deformations for applications in shape morphing in soft materials.

## 7. Summary and conclusions

We have presented a novel finite element framework for computational morphoelasticity by extending a state-of-the-art mixed displacement–pressure formulation recently proposed by two of the authors. The adapted mixed finite element formulation effectively accounts for compressible, nearly incompressible as well as truly incompressible behaviour in a single numerical framework. Quadratic and linear Bézier elements are employed for spatial discretisation. The novel contributions of the present work can be summarised as

- (i) the ability to accurately model the perfect incompressibility behaviour in morphoelasticity,
- (ii) inf–sup stable elements with different shapes in 2D and 3D to ease the task of mesh generation for problems with complex geometries,
- (iii) accurate capturing of stress discontinuities at the material interfaces using duplicated pressure DOFs, and
- (iv) study of the effect of hyperelastic material models and compressibility on growth-induced deformations.

The accuracy of the proposed finite element analysis framework is demonstrated first by comparing the numerical results with the corresponding analytical solutions for the examples of single- and multi-layered plates. These numerical examples demonstrate that accurate numerical solutions can be obtained with coarse meshes using the proposed elements; thus, illustrating the superiority of the high-order elements over the widely-used Q1/P0 element, especially for problems undergoing significant deformations due to the induced growth. Later, the effect of different hyperelastic constitutive models and compressibility on growth-induced deformations are assessed. It is observed that the effect of material models on the extent of deformation is negligible and that compressibility has a negative impact on the amount of bending deformation. Finally, growth-induced deformations in morphoelastic rods, flower petals, and thin cylindrical tubes are simulated to prove the potential of the proposed framework for complex problems.

To conclude, the ability to incorporate perfectly incompressible material models in combination with compressible models make the proposed finite element analysis framework a computationally appealing numerical simulation scheme for capturing morphoelasticity. The proposed work opens up numerous avenues for extensions in the future. A straightforward extension of the framework is to couple with the recently proposed procedure for computational electromechanics, for applications in electro- and/or magneto-active gels. Another possibility is to add the arc-length method and inflation techniques to predict the bifurcation points and post-buckling instabilities in soft layered composites.

## CRedit authorship contribution statement

**Chennakesava Kadapa:** Conceptualization, Formal analysis, Software, Original draft writing - review & editing. **Zhanfeng Li:** Investigation, Methodology, Original draft writing. **Mokarram Hossain:** Conceptualization, Formal analysis, Original draft writing - review & editing. **Jiong Wang:** Investigation, Methodology, Supervision.

**Declaration of competing interest**

The authors declare that they have no known competing financial interests or personal relationships that could have appeared to influence the work reported in this paper.

**Acknowledgements**

M. Hossain acknowledges the funding through an EPSRC Impact Acceleration Award (2020–2021), United Kingdom. J. Wang thanks the support from the National Natural Science Foundation of China (Project No.: 11872184).

**Appendix A. Formulation**

Starting from Eq. (32), the second variation ( $d$ ) of the total energy functional ( $\Pi$ ) can be written as

$$d(\delta \Pi) = \int_{B_0} \left[ \delta F_{iJ} \frac{\partial \bar{P}_{iJ}}{\partial F_{kL}} dF_{kL} J^g + p d(\delta J) + \delta p dJ + \delta J dp - J^g \hat{\vartheta} \delta p dp \right] dV - d(\delta \Pi_{\text{ext}}). \tag{A.1}$$

Using (21) and (34), we get

$$\begin{aligned} \delta F_{iJ} \frac{\partial \bar{P}_{iJ}}{\partial F_{kL}} dF_{kL} J^g &= \delta u_{i,j} F_{jJ} \frac{\partial \bar{P}_{iJ}}{\partial F_{kL}} F_{iL} du_{k,l} \frac{J}{J^e} \\ &= \delta u_{i,j} F_{jR}^e F_{RJ}^g \bar{\mathbb{D}}_{iQkN}^e F_{LN}^{g-1} F_{JQ}^{g-1} F_{iS}^e F_{SL}^g du_{k,l} \frac{J}{J^e} \\ &= \delta u_{i,j} \left[ J \bar{\mathbb{C}}_{ijkl}^e \right] du_{k,l}, \end{aligned} \tag{A.2}$$

$$\begin{aligned} d(\delta J) &= \delta F_{iJ} J \frac{\partial F_{Ji}^{-1}}{\partial F_{kL}} dF_{kL} + \delta F_{iJ} F_{Ji}^{-1} \frac{\partial J}{\partial F_{kL}} dF_{kL} \\ &= -\delta u_{i,j} F_{jJ} J F_{Jk}^{-1} F_{Li}^{-1} du_{k,l} F_{iL} + \delta u_{i,j} F_{jJ} F_{Ji}^{-1} J F_{Lk}^{-1} du_{k,l} F_{iL} \\ &= \delta u_{i,j} J \left[ \delta_{ji} \delta_{lk} - \delta_{jk} \delta_{il} \right] du_{k,l}. \end{aligned} \tag{A.3}$$

Now, the addition of the above two expressions yields,

$$\delta F_{iJ} \frac{\partial \bar{P}_{iJ}}{\partial F_{kL}} dF_{kL} J^g + p d(\delta J) = \delta u_{i,j} J \left[ \bar{\mathbb{C}}_{ijkl}^e + p \left[ \delta_{ij} \delta_{kl} - \delta_{jk} \delta_{il} \right] \right] du_{k,l} = \delta u_{i,j} J \mathbb{C}_{ijkl} du_{k,l} \tag{A.4}$$

where

$$\mathbb{C}_{ijkl} = \bar{\mathbb{C}}_{ijkl}^e + p \left[ \delta_{ij} \delta_{kl} - \delta_{jk} \delta_{il} \right]. \tag{A.5}$$

**Appendix B. Analytical solution**

*B.1. Multi-layered beam in plane-strain*

The analytical solution for the four-layered beam example in terms of the coordinates in the deformed configuration is given below.

First layer:

$$x = r \sin \left( \frac{15 \pi X}{16} \right), \quad y = r \cos \left( \frac{15 \pi X}{16} \right) - \frac{1408 + 109 \pi}{1200 \pi} \tag{B.1}$$

with

$$r = \frac{440 \pi [240 Y + 7] + \pi^2 [75 Y [13 - 600 Y] + 19] + 123904}{1200 \pi [88 + \pi]} \tag{B.2}$$

Second layer:

$$x = r \sin \left( \frac{15 \pi X}{16} \right), \quad z = r \cos \left( \frac{15 \pi X}{16} \right) - \frac{4 [1408 + 109 \pi]}{4800 \pi} \tag{B.3}$$

with

$$r = \frac{1760 \pi [240 Y + 13] + \pi^2 [181 - 4500 Y [40 Y - 1]] + 495616}{4800 \pi [88 + \pi]} \tag{B.4}$$

Third layer:

$$x = r \sin \left( \frac{15 \pi X}{16} \right), \quad y = r \cos \left( \frac{15 \pi X}{16} \right) - \frac{4 [1408 + 109 \pi]}{4800 \pi} \tag{B.5}$$

with

$$r = \frac{1760 \pi [240 Y + 19] + \pi^2 [300 Y [17 - 600 Y] + 301] + 495616}{4800 \pi [88 + \pi]} \quad (\text{B.6})$$

Fourth layer:

$$x = r \sin\left(\frac{15 \pi X}{16}\right), \quad y = r \cos\left(\frac{15 \pi X}{16}\right) - \frac{1408 + 109 \pi}{1200 \pi} \quad (\text{B.7})$$

$$r = \frac{2200 \pi [48 Y + 5] + \pi^2 [75 Y [19 - 600 Y] + 109] + 123904}{1200 \pi [88 + \pi]} \quad (\text{B.8})$$

## B.2. Analytical solution for the butterfly shape

The expressions for the coordinates for the butterfly shape in the deformed configuration are:

$$x = \frac{1}{2\sqrt{5}} \sin(\pi X) \left[1 + 4 \cos(\pi X)\right] + Y \frac{2 [\cos(\pi X) - \cos(2\pi X)]}{\sqrt{5} \sqrt{\cos(\pi X)^2 + 4 \cos(2\pi X)^2}} \quad (\text{B.9})$$

$$y = -\frac{1}{\sqrt{5}} \sin(\pi X) \left[1 - \cos(\pi X)\right] + Y \frac{\cos(\pi X) + 4 \cos(2\pi X)}{\sqrt{5} \sqrt{\cos(\pi X)^2 + 4 \cos(2\pi X)^2}} \quad (\text{B.10})$$

## References

- Ambrosi, D., Ateshian, G.A., Arruda, E.M., Cowin, S.C., Dumais, J., Goriely, A., Holzapfel, G.A., Humphrey, J.D., Kemkemer, R., Kuhl, E., Olberding, J.E., Taber, L.A., Garikipati, K., 2011. Perspectives on biological growth and remodeling. *J. Mech. Phys. Solids* 59, 863–883.
- Armstrong, M.H., Tepole, A.B., Kuhl, E., Simon, B.R., Vande Geest, J.P., 2016. A finite element model for mixed porohyperelasticity with transport, swelling, and growth. *PLoS ONE* 11 (4), e0152806.
- Audoly, B., Boudaoud, A., 2008. Buckling of a stiff film bound to a compliant substrate: part I-III. *J. Mech. Phys. Solids* 56, 2401–2458.
- Ben Amar, M., Goriely, A., 2005. Growth and instability in elastic tissues. *J. Mech. Phys. Solids* 53, 2284–2319.
- Bonnet, J., Wood, R.D., 1997. *Nonlinear Continuum Mechanics for Finite Element Analysis*. Cambridge University Press, Cambridge.
- Brezzi, F., Fortin, M., 1991. *Mixed and Hybrid Finite Element Methods*. Springer-Verlag, New York.
- Budday, S., Andres, S., Walter, B., Steinmann, P., Kuhl, E., 2017. Wrinkling instabilities in soft bilayered systems. *Phil. Trans. R. Soc. A* 375, 21060163.
- Budday, S., Steinmann, P., Kuhl, E., 2014. The role of mechanics during brain development. *J. Mech. Phys. Solids* 72, 75–92.
- Cai, S., Breid, D., Crosby, Z., Suo, A.J., Hutchinson, J.W., 2011. Periodic patterns and energy states of buckled films on compliant substrates. *J. Mech. Phys. Solids* 59, 1094–1114.
- Cao, Y.P., Hutchinson, J.W., 2012. From wrinkles to creases in elastomers: the instability and imperfection-sensitivity of wrinkling. *Proc. R. Soc. A* 468, 94–115.
- Coen, E., Rolland-Lagan, A.G., Matthews, M., Bangham, J.A., Prusinkiewicz, P., 2004. The genetics of geometry. *Proc. Natl. Acad. Sci.* 101, 4728–4735.
- Dai, H.H., Song, Z.L., 2014. On a consistent finite-strain plate theory based on a 3-D energy principle. *Proc. R. Soc. A* 470, 20140494.
- Dervaux, J., Ciarletta, P., Ben Amar, M., 2009. Morphogenesis of thin hyperelastic plates: a constitutive theory of biological growth in the Föppl-von Kármán limit. *J. Mech. Phys. Solids* 57, 458–471.
- Dortdivanlioglu, B., Javili, A., Linder, C., 2017. Computational aspects of morphological instabilities using isogeometric analysis. *Comput. Methods Appl. Mech. Engrg.* 316, 261–279.
- Dortdivanlioglu, B., Linder, C., 2019. Diffusion-driven swelling-induced instabilities of hydrogels. *J. Mech. Phys. Solids* 125, 38–52.
- Du, P., Dai, H.H., Wang, J., Wang, Q.Y., 2020. Analytical study on growth-induced bending deformations of multi-layered hyperelastic plates. *Int. J. Non-Linear Mech.* 119, 103370.
- Egunov, A.I., Korvink, J.G., Luchnikov, V.A., 2016. Polydimethylsiloxane bilayer films with embedded spontaneous curvature. *Soft Matter* 12, 45–52.
- Garcia-Gonzalez, D., Jerusalem, A., 2019. Energy based mechano-electrophysiological model of CNS damage at the tissue scale. *J. Mech. Phys. Solids* 125, 22–37.
- Garcia-Gonzalez, D., Jerusalem, A., Garzon-Hernandez, S., Zaera, R., Arias, A., 2018. A continuum mechanics constitutive framework for transverse isotropic soft tissues. *J. Mech. Phys. Solids* 112, 209–224.
- Geuzaine, C., Remacle, J.-F., 2009. Gmsh: a three-dimensional finite element mesh generator with built-in pre- and post-processing facilities. *Internat. J. Numer. Methods Engrg.* 79, 1309–1331.
- Green, P.B., 1996. Transductions to generate plant form and pattern: an essay on cause and effect. *Ann. Botany* 78, 269–281.
- Guennebaud, G., Jacob, B., et al., 2010. *Eigen v3*. (<http://eigen.tuxfamily.org>).
- Holmes, D.P., 2019. Elasticity and stability of shape-shifting structures. *Curr. Opin. Colloid Interface Sci.* 40, 118–137.
- Holmes, D.P., Roche, M., Sinha, T., Stone, H.A., 2011. Bending and twisting of soft materials by non-homogenous swelling. *Soft Matter* 7, 5188.
- Hossain, M., Kabir, N., Amin, A.F.M.S., 2015. Eight-chain and full-network models and their modified versions for rubber hyperelasticity: A comparative study. *J. Mech. Behav. Mater.* 24 (1–2), 11–24.
- Hossain, M., Possart, G., Steinmann, P., 2010. A finite strain framework for the simulation of polymer curing. Part II. Viscoelasticity and shrinkage. *Comput. Mech.* 46, 363–375.
- Hossain, M., Steinmann, P., 2013. More hyperelastic models for rubber-like materials: Consistent tangent operator and comparative study. *J. Mech. Behav. Mater.* 22 (1–2), 27–50.
- Ilseng, A., Prot, V., Skallerud, B.H., Stokke, B.T., 2019. Buckling initiation in layered hydrogels during transient swelling. *J. Mech. Phys. Solids* 128, 219–238.
- Ionov, L., 2013. Biomimetic hydrogel-based actuating systems. *Adv. Funct. Mater.* 23, 4555–4570.
- Jones, G.W., Chapman, S.J., 2012. Modeling Growth in Biological Materials. *SIAM Rev.* 54, 52–118.
- Kadapa, C., 2014. Mixed Galerkin and Least-Squares Formulations for Isogeometric Analysis (Ph.D. thesis). College of Engineering, Swansea University.
- Kadapa, C., 2019a. Novel quadratic Bézier triangular and tetrahedral elements using existing mesh generators: Applications to linear nearly incompressible elastostatics and implicit and explicit elastodynamics. *Internat. J. Numer. Methods Engrg.* 117, 543–573.
- Kadapa, C., 2019b. Novel quadratic Bézier triangular and tetrahedral elements using existing mesh generators: Extension to nearly incompressible implicit and explicit elastodynamics in finite strains. *Internat. J. Numer. Methods Engrg.* 119, 75–104.

- Kadapa, C., 2020. A novel semi-implicit scheme for elastodynamics and wave propagation in nearly and truly incompressible solids. *Acta Mech.* in press.
- Kadapa, C., Dettmer, W.G., Perić, D., 2016. Subdivision based mixed methods for isogeometric analysis of linear and nonlinear nearly incompressible materials. *Comput. Methods Appl. Mech. Engrg.* 305, 241–270.
- Kadapa, C., Hossain, M., 2020a. A linearized consistent mixed displacement-pressure formulation for hyperelasticity. *Mech. Adv. Mater. Struct.*
- Kadapa, C., Hossain, M., 2020b. A robust and computationally efficient finite element framework for coupled electromechanics. *Comput. Methods Appl. Mech. Engrg.* 372, 113443.
- Kempaiah, R., Nie, Z.H., 2014. From nature to synthetic systems: shape transformation in soft materials. *J. Mater. Chem. B* 2, 2357–2368.
- Khang, D.Y., Rogers, J.A., Lee, H.H., 2009. Mechanical buckling: Mechanics, metrology, and stretchable electronics. *Adv. Funct. Mater.* 19, 1526–1536.
- Kourounis, D., Fuchs, A., Schenk, O., 2018. Towards the next generation of multiperiod optimal power flow solvers. *IEEE Trans. Power Syst.* 99, 1–10.
- Kuhl, E., 2014. Growing matter: A review of growth in living systems. *J. Mech. Behav. Biomed. Mater.* 29, 529–543.
- Kuhl, E., Menzel, A., Steinmann, P., 2003. Computational modeling of growth. A critical review, a classification of concepts and two new consistent approaches. *Comput. Mech.* 32, 71–88.
- Lanir, Y., 2015. Mechanistic micro-structural theory of soft tissues growth and remodeling: tissues with unidirectional fibers. *Biomech. Model. Mechanobiol.* 14, 245–266.
- Lessinnes, T., Moulton, D.E., Goriely, A., 2017. Morphoelastic rods Part II: Growing birods. *J. Mech. Phys. Solids* 100, 147–196.
- Li, B., Cao, Y.P., Feng, X.Q., Gao, H.J., 2012. Mechanics of morphological instabilities and surface wrinkling in soft materials: A review. *Soft Matter* 8, 5728–5745.
- Li, B., Xu, G.K., Feng, X.Q., 2013. Tissue-growth model for the swelling analysis of core-shell hydrogels. *Soft Matter* 11, 117–124.
- Liu, Y., Genzer, J., Dickey, M.D., 2016. 2D or not 2D: shape-programming polymer sheets. *Prog. Polym. Sci.* 52, 79–106.
- Lubarda, V.A., Hoger, A., 2002. On the mechanics of solids with a growing mass. *Int. J. Solids Struct.* 39, 4627–4664.
- Menzel, A., Kuhl, E., 2012. Frontiers in growth and remodeling. *Mech. Res. Commun.* 42, 1–14.
- Mora, T., Boudaoud, A., 2006. Buckling of swelling gels. *Eur. Phys. J. E* 20, 119–124.
- Moulton, D.E., Goriely, A., 2011. Circumferential buckling instability of a growing cylindrical tube. *J. Mech. Phys. Solids* 59, 525–537.
- Moulton, D.E., Lessinnes, T., Goriely, A., 2013. Morphoelastic rods. Part I: A single growing elastic rod. *J. Mech. Phys. Solids* 61, 398–427.
- Moulton, D.E., Lessinnes, T., Goriely, A., 2020. Morphoelastic rods III: Differential growth and curvature generation in elastic filaments. *J. Mech. Phys. Solids* 142, 104022.
- Nash, M.P., Hunter, P.J., 2000. Computational mechanics of the heart. *J. Elasticity* 61, 113–141.
- Nath, U., Crawford, B.C.W., Carpenter, R., Coen, E., 2003. Genetic control of surface curvature. *Science* 299, 1404–1407.
- Ogden, R.W., 1997. *Non-Linear Elastic Deformation*. Dover Publications, New York.
- Pezzulla, M., Smith, G.P., Nardinocchi, P., Holmes, D.P., 2016. Geometry and mechanics of thin growing bilayers. *Soft Matter* 12, 4435.
- Rausch, M.K., Kuhl, E., 2013. On the effect of prestrain and residual stress in thin biological membranes. *J. Mech. Phys. Solids* 61, 1955–1969.
- Raybaud, C., Widjaja, E., 2011. Development and dysgenesis of the cerebral cortex: malformations of cortical development. *Neuroimaging Clin. N. Am.* 21 (3), 483–543.
- Reese, S., Govindjee, S., 1998. A theory of finite viscoelasticity and numerical aspects. *Int. J. Solids Struct.* 35 (26–27), 3455–3482.
- Rodriguez, A.K., Hoger, A., McCulloch, A., 1994. Stress-dependent finite growth in soft elastic tissue. *J. Biomech.* 27, 455–467.
- Skalak, R., Zargaryan, S., Jain, R.K., Netti, P.A., Hoger, A., 1996. Compatibility and the genesis of residual stress by volumetric growth. *J. Math. Biol.* 34, 889–914.
- Stafford, C.M., Harrison, C., Beers, K.L., Karim, A., Amis, E.J., Van Landingham, M.R., Kim, H.C., Volksen, W., Miller, R.D., Simonyi, E.E., 2004. A buckling-based metrology for measuring the elastic moduli of polymeric thin films. *Nature Mater.* 3, 545–550.
- Steinmann, P., Hossain, M., Possart, G., 2012. Hyperelastic models for rubber-like materials: Consistent tangent operators and suitability of Treloar's data. *Arch. Appl. Mech.* 82 (9), 1183–1217.
- Sultan, E., Boudaoud, A., 2008. The buckling of a swollen thin gel layer bound to a compliant substrate. *J. Appl. Mech.* 75, 051002.
- Terwagne, D., Brojan, M., Reis, P.M., 2014. Smart morphable surfaces for aerodynamic drag control. *Adv. Mater.* 26, 6608–6611.
- Wang, J., Dai, H.H., Song, Z.L., 2016. On a consistent finite-strain plate theory for incompressible hyperelastic materials. *Int. J. Solids Struct.* 78–79, 101–109.
- Wang, J., Steigmann, D., Wang, F.F., Dai, H.H., 2018a. On a consistent finite-strain plate theory of growth. *J. Mech. Phys. Solids* 111, 184–214.
- Wang, J., Wang, Q., Dai, H.H., 2018b. Stress-free bending of a neo-Hookean plate induced by growth: Exact solution and experiments. *Int. J. Non-Linear Mech.* 106, 280–287.
- Wang, J., Wang, Q.Y., Dai, H.H., Du, P., Chen, D.X., 2019. Shape-programming of hyperelastic plates through differential growth: An analytical approach. *Soft Matter* 15, 2391–2399.
- Wang, J., Zhang, H., Zheng, Y., Ye, H., 2020. High-order NURBS elements based isogeometric formulation for swellable soft materials. *Comput. Methods Appl. Mech. Engrg.* 363, 112901.
- Xu, F., Fu, C., Yang, Y., 2020. Water affects morphogenesis of growing aquatic plant leaves. *Phys. Rev. Lett.* 124, 038003.
- Xu, F., Koutsawa, Y., Potier-Ferry, M., Belouettar, S., 2015. Instabilities in thin films on hyperelastic substrates by 3D finite elements. *Int. J. Solids Struct.* 69–70, 71–85.
- Xu, F., Potier-Ferry, M., Belouettar, S., Cong, Y., 2014. 3D finite element modeling for instabilities in thin films on soft substrates. *Int. J. Solids Struct.* 51, 3619–3632.
- Yuk, H., Lin, S., Ma, C., Takaffoli, M., Fang, N.X., Zhao, X., 2017. Hydraulic hydrogel actuators and robots optically and sonically camouflaged in water. *Nature Commun.* 8, 14230.
- Zhao, R., Zhang, T., Diab, M., Gao, H., Kim, K.-S., 2015. The primary bilayer ruga-phase diagram I: Localizations in ruga evolution. *Extreme Mech. Lett.* 4, 76–82.
- Zhou, Z., Li, Y., Guo, T.F., Guo, X., Tang, S., 2018. Surface instability of bilayer hydrogel subjected to both compression and solvent absorption. *Polymers* 10, 624.
- Zienkiewicz, O.C., Taylor, R.L., Fox, D.D., 2014. *The Finite Element Method for Solid and Structural Mechanics*, seventh ed. Butterworth and Heinemann.